ANL-76-110

CRACKING AND HEALING BEHAVIOR OF UO_2 AS RELATED TO PELLET-CLADDING MECHANICAL INTERACTION

Interim Report

July 1976

by

C. R. Kennedy, F. L. Yaggee, J. C. Voglewede,
D. S. Kupperman, B. J. Wrona, W. A. Ellingson,
E. Johanson, and A. G. Evans

U of C-AUA-USERDA

ARGONNE NATIONAL LABORATORY, ARGONNE, ILLINOIS

Prepared for the U. S. ENERGY RESEARCH
AND DEVELOPMENT ADMINISTRATION
under Contract W-31-109-Eng-38

Printed in the United States of America
Available from
National Technical Information Service
U. S. Department of Commerce
5285 Port Royal Road
Springfield, Virginia 22161
Price: Printed Copy $4.50; Microfiche $3.00

Distribution Categories:
Materials (UC-25)
LWR Technology (UC-78)
General Reactor Technology
(UC-80)

ANL-76-110

ARGONNE NATIONAL LABORATORY
9700 South Cass Avenue
Argonne, Illinois 60439

CRACKING AND HEALING BEHAVIOR OF UO_2 AS RELATED TO PELLET-CLADDING MECHANICAL INTERACTION

Interim Report
July 1976

by

C. R. Kennedy, F. L. Yaggee, J. C. Voglewede,
D. S. Kupperman, B. J. Wrona, W. A. Ellingson,
E. Johanson,* and A. G. Evans**

Materials Science Division

October 1976

Prepared for the Electric Power Research Institute
Palo Alto, California
Contract #RP508-1

*Electronics Division, ANL.
**Rockwell International, Thousand Oaks, California 91360.

TABLE OF CONTENTS

LIST OF FIGURES

LIST OF FIGURES (Contd.)

LIST OF TABLES

CRACKING AND HEALING BEHAVIOR OF UO_2 AS RELATED TO PELLET-CLADDING MECHANICAL INTERACTION

Interim Report
July 1976

by

C. R. Kennedy, F. L. Yaggee, J. C. Voglewede, D. S. Kupperman, B. J. Wrona, W. A. Ellingson, E. Johanson, and A. G. Evans

ABSTRACT

A direct-electrical-heating apparatus has been designed and fabricated to investigate those nuclear-fuel-related phenomena involved in the gap closure-bridging annulus formation mechanism that can be reproduced in an out-of-reactor environment. Prototypic light-water-reactor UO_2 fuel-pellet temperature profiles have been generated utilizing high flow rates ($\sim$700 liters/min) of helium coolant gas, and a recirculating system has been fabricated to permit tests of up to 1000 h.

Simulated light-water-reactor single- and multiple-thermal-cycle experiments will be conducted on both unclad and ceramic (fused silica) clad UO_2 pellet stacks.

A laser dilatometer with a resolution of 1.27×10^{-2} mm (5×10^{-4} in.) will be used to measure pellet dimensional increase continuously during thermal cycling. Acoustic emissions from thermal-gradient cracking have been detected and correlated with crack length and crack area. The acoustic emissions will be monitored continuously to provide instantaneous information about thermal-gradient cracking. In addition, posttest metallography and fracture-mechanics measurements will be utilized to characterize cracking and crack healing.

I. INTRODUCTION

A. Background

Pellet-cladding mechanical interaction (PCMI) can result in fuel-rod failure (development of throughwall cladding cracks) during power increases in the Zircaloy-clad UO_2 fuel rods currently employed in light-water reactors (LWRs). A reduction in the rates of power change, in an attempt to lower interaction stresses, would result in a decrease of plant capacity. An excess of cladding perforations can cause shutdowns or deratings in boiling water reactors (BWRs) because of the limitations on stack-gas emissions. In addition, radionuclides that escape through cladding perforations into the primary-loop coolant increase radiation fields and render equipment maintenance difficult in both BWRs and pressurized water reactors (PWRs). Thus, a significant

economic incentive exists to understand the phenomena and either mitigate their effects by design or optimize the fuel duty cycle to minimize associated costs.

The ultimate driving force that produces the cladding failure is the result of the differential thermal expansion between the fuel and cladding during a power increase. However, an understanding of a prior link in the mechanistic chain, i.e., the mechanism responsible for closing the fuel-cladding gap and forming a structural bridging annulus within the fuel, is not well established. This process, whether operating on the initial (fabricated) gap or on a gap produced as the result of a power decrease, sets the stage for subsequent PCMI by the differential thermal-expansion mechanism.

B. Project Description

The present project is designed to investigate those fuel-related phenomena believed to be involved in the gap closure-bridging annulus formation mechanism that can be reproduced in the out-of-reactor environment provided by the direct-electrical-heating (DEH) apparatus at Argonne National Laboratory (ANL). Data from this program will be supplied to Entropy Limited (EL), Lincoln, MA, for additional analysis under EPRI contract number RP508-2. Entropy Limited will apply an information theoretical base approach to the development of a statistical model of crack formation and related effects on UO_2 nuclear fuel as a function of heating rates, temperature profiles, number of cycles, and other variables measured during the ANL experimental project. These results will be complemented by in-reactor experiments to be run in the Halden Reactor.

Specific program objectives at ANL are to

1. Investigate the occurrence of cracking and healing during the first power cycle of an unirradiated fuel column. Record the manifestations of the cracking and crack-healing processes in terms of microstructural changes and external dimensional changes.

2. Investigate the effects of thermal cycling on the microstructure and exterior dimensions of an unclad fuel column.

3. Investigate the effects of thermal cycling and vibration on PCMI and microstructure in a clad fuel column.

4. Determine the importance of thermal gradient in the crack-healing process.

In addition, a subcontract to Rockwell International (RI), Thousand Oaks, CA, will permit acquisition of fundamental fracture-mechanics data for UO_2.

II. PROJECT IMPLEMENTATION

A. DEH Specimen Chamber *(F. L. Yaggee, B. J. Wrona, and C. R. Kennedy)*

Fabrication and testing of the DEH specimen chamber have been completed. The assembled chamber is shown in Fig. 1. Note that the UO_2 pellet stack (which consists of seven pellets) is surrounded by a quartz cylinder

("chimney") and baffle designed to channel the helium coolant gas onto the pellets. Electrical contact is accomplished through tungsten electrodes held in place by upper and lower water-cooled brass electrode holders. These assemblies can carry currents in excess of 100 A and are insulated from the specimen-chamber body by lava insulators capable of withstanding 2500 V. To account for axial displacement during temperature-cycling experiments, the upper electrodes have been spring loaded. Four windows provide visual access and enable the pellet surface temperature to be measured by infrared pyrometers and the diametral expansion or contraction to be measured by a laser dilatometer system. Vibration can be applied to the pellet stack by attaching to the specimen chamber a commercial compressed air-driven vibrator that employs a ball bearing rotating in a race. Acoustic-emission transducers have been mounted on metal extensions of the upper and lower electrodes and are capable of detecting the acoustic waves generated by the thermal-gradient cracking of the UO_2 pellets.

B. DEH Power Supply *(E. Johanson, B. J. Wrona, and C. R. Kennedy)*

The DEH power supply, similar to that of Wrona et al.[1] and Wrona and Johanson,[2] has been constructed and tested. It consists of two power supplies that operate in parallel. In the low-voltage, high-current power supply (300 V and 300 A) and the high-voltage, low-current power supply (2500 V and 10 A), the positive terminals are decoupled by diodes. When the resistance of the UO_2 pellet stack is such that the potential drop across the stack exceeds 300 V, the diodes back-bias and limit the current drawn from the high-voltage power supply. Current can be drawn from both the low-voltage and high-voltage power supply when the voltage drop across the pellet stack is <300 V. At room temperature, the electrical resistance of UO_2 is quite high; however, as the temperature increases, the resistivity decreases rapidly. Hence, the high-voltage power supply serves to initiate current flow in the pellet stack in lieu of an external heating device. Voltage-limiting, current-limiting, and power-limiting controls serve to regulate the power input to the stack, with a Data Trak programmer used to provide reproducible power ramps from 1 to 10,000 min duration. Data acquisition will be accomplished during steady-state operations through the use of a 24-point multichannel strip-chart recorder, whereas a Wang minicomputer will also be utilized during periods when the power or other input parameters are rapidly changing.

C. Gas-coolant System *(F. L. Yaggee)*

The purpose of the helium loop is to provide a continuous flow of helium coolant gas to the DEH test chamber, where it is used to establish and maintain a large radial temperature gradient within a UO_2 fuel-pellet stack.

The closed gas system consists of an oilless (Corken) compressor, a 227-liter (8 cu ft) gas receiver tank, a helium loop, a test chamber, and a 227-liter expansion tank that provides the inlet gas to the compressor (Fig. 2). The closed gas system, excluding test chamber, is charged initially with bottled helium gas (99.99% pure). During operation of the DEH apparatus, the compressor provides a constant supply (227 liters) of 5.17×10^5 N/m^2 (75 psig) helium gas, which flows through the helium loop before entering the test chamber. The helium gas is continuously purified within the loop by passing a regulated portion of the main gas stream through activated carbon and

molecular sieve traps at liquid nitrogen temperature and through a high-temperature gettering furnace. Capabilities of the helium loop include test-chamber operating pressures up to 4.14×10^5 N/m^2 (60 psig) and regulated helium flow rates up to 991 actual liters/min (35 actual cfm) at a chamber pressure of $\sim 2.76 \times 10^5$ N/m^2 (40 psig). Accurate and reproducible helium flow-rate control is achieved by a unique regulator valve design that uses an oscillator-controlled step-motor drive. Provision is made for the continuous control and recording of the helium flow rate and oxygen and moisture impurities in the helium gas. The helium loop system also incorporates such automatic features as test-chamber depressurization for inspection and replacement of the pellet stack, test-chamber purging prior to the start of a DEH run, makeup gas injection, and change in the compressor duty cycle with flow rate through the test chamber.

The helium loop is expected to extend individual DEH test runs from the present 10 to 15-min maximum to several hundred hours. Under steady-state test conditions, the helium loop can be run unattended overnight, and it will shut down in a fail-safe manner in the event of a power or cooling-water failure. The gas-cooling system is expected to be operational in early September.

D. Instrumentation and Data Acquisition *(J. C. Voglewede)*

The DEH instrumentation panel is shown in Fig. 3. This panel contains most of the instrumentation output modules and electrical controls that will be utilized in the upcoming experiments.

Table I is a tentative list of inputs to the multichannel chart recorder. Note that they need not all be used at the same time. When an input is not being recorded, the respective channel will be bypassed. For example, every time channel 2 is recorded, it indicates only the root-mean-square (rms) voltage level. Since the recorder can accommodate up to 24 channels, new data channels may be added as necessary. The multichannel chart recorder input range is fixed at 0-10 V direct current (dc) with a sampling rate of ~ 5 s per channel. The input impedance of 10^4 Ω is being upgraded to 10^5 Ω with an isolation amplifier to eliminate loading.* During some phases of the testing, certain data channels will also be recorded by computer. These inputs will be recorded along with a header label that contains, for example, sample identification and dimensions. The input data are tentatively identified as shown in Table II. The raw data input to the computer system will be identical to the 0-10 V dc signals recorded by the multichannel chart recorder. All scan intervals will be 0.1, 1.0, or 10.0 min as requested by EL. The scan interval may be changed during the test.

A fundamental difference between computer and multipoint recorder scanning should be noted. The multichannel chart recorder samples a single channel of data and, after an ~ 5-s pause, samples the next selected channel. A scan of a number of selected channels is repeated over and over with the same 5-s pause between scans. Absolute time measurements are deduced from chart-paper displacement.

*When specific electronic data are quoted, it should be considered that components and their values may change as a result of experimental considerations.

TABLE I. Data Input to Multichannel Recorder

Channel	Input	
1	Rms current	
2	Rms voltage	
3	Rms power	
4	Selector switch	
5	IRCON Model 300 (70 to 2800°C -- nine ranges)	Pyrometers
6	IRCON No. 1 (400 to 1000°C -- single range)	
7	IRCON No. 2 (900 to 1600°C -- single range)	
8	IRCON No. 3 (1500 to 3000°C -- single range)	
9	Acoustic-emission integrated rms signal	
10	Acoustic-emission event or integrator reset count	
11	RETICON -- diametral measurement	
12	RETICON -- axial position	
13	Linear Variable Differential Transformer (LVDT) -- axial displacement	
14	Gas flow rate	
15	H_2O level in gas stream	
16	Thermox (O_2 level in gas stream)	

TABLE II. Data Input to Computer

Channel	Input	
1	Rms current	
2	Rms voltage	
3	Selector switch	
4	IRCON No. 1	Pyrometers
5	Any other IRCON	
6	Acoustic-emission integrated rms signal	
7	LVDT/load cell -- axial displacement/force	
8	RETICON -- diametral measurement	
9	Gas flow rate	
10	Time (hours, minutes, and seconds)	

With the computer-driven data-acquisition system, the scan of a number of selected channels takes only a few hundred microseconds. The interval between scans (0.1, 1.0, or 10.0 min) is precisely determined by a quartz oscillator clock. In other words, the time base for the computer-recorded signals is rigidly controlled and that of the multipoint recorder is not. Within the following sections, the various inputs for each channel are identified and described.

1. Rms Current

The rms current is a measure of the effective electrical current passing through the pellet stack. The current is derived from either the high- or low-voltage power supply shown in Fig. 4. Each power supply is a three-phase silicon-controlled-rectifier (SCR) fired arrangement that provides a rapid series of power bursts synchronized with the line frequency. The current and voltage measured at the pellet stack is therefore a rapid series of power pulses, as observed in Fig. 5. This figure shows a 600-V alternating current (ac) component superimposed on a 200-V dc level. The result is an effective or rms value of ∿500 V. This waveform results at zero current flow through the stack. As more current is drawn, the ac component of the waveform decreases as a result of capacitive and inductive filtering in the power supply.

Burr-Brown Model 4340 true rms-to-dc converters are used to provide effective current and voltage values. These converters have 22-μF external capacitors to extend the low-frequency response of the units. Frequency response and calibration of the units have been performed with the positive component of square-wave and sinusoidal signals. The noise level of the output signal as a function of frequency is shown in Fig. 6. The input signal in this case is a 0 to +10-V square wave. The resultant dc output signal at higher frequencies is 7.07 V, which is the expected rms value of a 0 to +10-V square wave.

As an example of the operation of the rms converter, the output of this unit is shown in Fig. 7 for the input used in Fig. 5. Figure 7 shows a nearly constant 5-V output from the unit (which corresponds to 500 V rms on the 1000-V scale). The ac component of the output is shown in Fig. 8. The magnitude of the ripple is ∿60 mV peak to peak.

The current level is derived from a 50-mV, 100-A shunt (labeled R_4 in Fig. 4). Since the shunt is wired in series with the pellet stack, any current that passes through the stack must also pass through the shunt. The shunt was calibrated in the 0 to 5-A range using a Leeds and Northrup Model 8686 mV potentiometer and Weston Model 370 precision ammeter (rated at $\frac{1}{4}$% full-scale reading). Calibration over the 0 to 30-A range was performed with a Wolff 0.001-Ω precision resistor and the potentiometer. In both cases, a Hewlett-Packard Model 6428B dc power supply was used. Data and results of the current shunt calibration are listed in Table III. The calibration yielded a shunt value of 1.995 A/mV.

The millivolt-to-volt conversion of the shunt signal is also performed in the rms indicator chassis. Since the gain is adjustable, the unit is calibrated for a set of millivolt input signals as shown in Table IV. The tabulated output signal is the signal recorded by the computer or multichannel

TABLE III. Current Shunt Calibration[a]

Weston Model 370, A	Wolff Standard Resistance, A	Shunt, mV
1.00	-	0.502, 0.503
2.00	-	1.008, 1.006
2.50	-	1.251, 1.257
3.00	-	1.507, 1.509
4.00	-	2.014, 2.012
5.00	-	2.516, 2.515
-	5.033	2.512
-	10.017	5.015
-	15.011	7.520
-	20.030	10.040
-	25.069	12.569
-	30.012	15.055

[a]Linear regression: $I_S = 1.99481\ X - 0.00475$, where I_S is the shunt current, and X is the shunt output.

TABLE IV. Rms Current Calibration[a]

Input, mV	Rms Range, A				
	10	20	50	100	200
0	0.014	0.012	0.010	0.010	0.010
5	10.00	5.00	2.01	1.008	0.509
10	-	10.00	4.00	2.01	1.01
25	-	-	9.99	5.00	2.50
50	-	-	-	9.99	5.00
100	-	-	-	-	9.99

[a]Output in volts.

recorder. The relation of output signal to sample current may be expressed as

$$I_X = 1.995\ X_I R_I / 20\ , \tag{1}$$

where I_X is the sample current in amperes, X_I is the current output signal in volts, and R_I is the current setting on the rms chassis (10, 20, 50, 100, or 200 A).

2. Rms Voltage

The voltage that appears across the sample stack at low current values has been shown in Fig. 5. Since the load as sensed by the power supply is almost totally resistive, the current and voltage waveforms are nearly identical. Each is composed of an ac and dc component. The greatest deviation from a pure dc signal occurs at low current levels (e.g., when the pellet stack is cold). Missed or unequal power bursts result from operating the high-voltage SCR power supply at low load levels. This causes high peak-to-rms signal levels. These problems have been greatly reduced with ballast loading (R_1 in Fig. 4) and by including an LC* filter in the high-voltage power-supply circuitry.

As was the case with the complex current waveform, conversion to effective voltage is accomplished with a second Burr-Brown Model 4340 true rms-to-dc converter in the rms chassis. The low-frequency response has again been extended with a 22-μF external capacitor. As long as a reasonably low peak-to-rms signal ratio is maintained, the conversion to effective voltage should be acceptable.

The voltage sense is obtained from the positive side of the DEH apparatus as shown in Fig. 4. Since the rms chassis senses the potential difference between this point and ground, the experimental value is actually the sum of the voltage drops across the pellet stack, pellet electrodes, power cables between the power supply and the experimental fixture, and the current shunt. Voltage drop due to components other than the pellet stack can be determined by running the apparatus with the electrodes shorted together (i.e., no pellet stack). Calibration runs performed in this fashion are shown in Table V. This table shows a voltage drop P of ∿31.6 mV per ampere of current flowing in the circuit. This is equivalent to 31.6 mΩ of resistance that results from system components other than the sample. The exact value changes for different electrode sizes and must be periodically checked. The voltage measurements can now be corrected for voltage drops once the current is known.

Conversion of the stack voltage to an output signal is again performed in the rms chassis. Calibration is necessary since the gain of the unit is adjustable. A Kepco regulated high-voltage dc power supply was used to simulate the input signal for the calibration. The results are listed in Table VI.

---

*L = 0.01 H, 12.5 A, 0.11 Ω, and 1500 V dc; C = 1.0 μF.

TABLE V. Voltage Drop Calibration[a]

Current, A	Voltage Drop, V
10	0.329
10	0.325
20	0.658
20	0.652
25	0.800
25	0.813
40	1.286
40	1.273
40	1.273
40	1.288
40	1.278

[a]Linear regression: $P = 0.0316\,I + 0.0155$.

TABLE VI. Rms Voltage Calibration

Input, V	Rms Range, V					
	50	100	200	500	1000	2000
0	0.006	0.004	0.002	0.002	0.002	0.002
50	9.99	5.00	2.50	0.998	0.500	0.251
100	-	10.00	5.00	2.00	0.997	0.500
200	-	-	9.99	4.00	2.00	1.001
500	-	-	-	10.00	5.00	2.50
1000	-	-	-	-	10.00	5.01
2000	-	-	-	-	-	10.00

The relationship of output signal to stack voltage may now be expressed as

$$U = X_V R_V / 10 - 0.0316\,I\,, \qquad (2)$$

where U is the stack voltage in volts, X_V is the voltage output signal in volts, and R_V is the voltage setting on the rms chassis (50, 100, 200, 500, 1000, or 2000 V).

3. Rms Power

The rms power level is obtained by electronically multiplying the rms current and rms voltage signals with a Burr-Brown 4204J multiplier. This unit may generate inaccurate results when either input level is near zero (e.g., current levels at start-up). The output is therefore not recorded by the computer-driven data-acquisition system, in which power is derived numerically. However, the power signal monitored by the multichannel recorder may be interpreted according to the relation

$$w = X_w R_V R_I \Big/ 10 , \tag{3}$$

where w is the power generated in the stack in watts and X_w is the power output signal in volts. It should be noted that the power signal is dependent on both the current and voltage settings of the rms chassis. Full-scale readings of as high as 400,000 W are possible on the instrument (although highly unlikely with the pellet stack).

4. Selector Switch

As was mentioned previously, the current, voltage, and power signals are related to the switch settings on the front of the rms chassis. In the case of current, the signal level may correspond to 10, 20, 50, 100, or 200 A full scale. In the case of voltage, the signal may correspond to 50, 100, 200, 500, 1000, or 2000 V full scale. The full-scale power signal will correspond to any combination of the above two sets of values. Multiple switch settings result in greater accuracy, but the switch positions must be changed during the test. A selector-switch channel has therefore been introduced to generate a different signal level for each unique combination of current and voltage setting. The output for this channel is shown in Table VII. The values of the low-order digits have been set high to avoid round-off error. Note that the high-order digit determines the voltage setting and the second highest order digit determines the current setting.

TABLE VII. Rms Selector-switch Calibration[a]

Voltage Setting, V	Current Setting, A				
	10	20	50	100	200
50	1.057	1.266	1.464	1.664	1.863
100	2.05	2.26	2.46	2.66	2.86
200	3.06	3.26	3.47	3.67	3.87
500	4.06	4.26	4.47	4.66	4.86
1000	5.07	5.27	5.47	5.67	5.87
2000	6.05	6.26	6.46	6.66	6.86

[a]Output in volts.

5. IRCON Model 300

The IRCON Model 300 infrared pyrometer responds to radiation in the 2.0 to 2.6-μm range. It is capable of measuring temperature from 70 to 2800°C in nine overlapping ranges. Unlike the other pyrometers used in this experiment, no unambiguous means exist of relating instrument output to temperature because of the different ranges involved. Calibration has been performed for three of the lower ranges by subjecting temperature and instrument output data to multiple-regression analysis. The fourth-order equations for each of these ranges (C-E) are

$$\text{Range C:}\quad T(°C) = 226.406 + 195.350X - 142.523X^2 + 44.2289X^3 \quad (227\text{-}343°C), \tag{4}$$

$$\text{Range D:}\quad T(°C) = 282.516 + 233.725X - 164.759X^2 + 50.5085X^3 \quad (283\text{-}427°C), \tag{5}$$

$$\text{Range E:}\quad T(°C) = 363.274 + 315.020X - 217.692X^2 + 67.6222X^3 \quad (366\text{-}566°C), \tag{6}$$

where X is the instrument output in volts and lies in the range 0.02-1.45 V. It should be noted that the output of this pyrometer is highly nonlinear. The utility of this pyrometer lies in its ability to measure extremely low surface temperatures. The IRCON Model 300, like the other pyrometers, has a built-in correction for emissivity, ε, that may be set anywhere in the range $0.2 \leq \varepsilon \leq 1.0$. The setting of the instrument is equivalent to effective emissivity, a combination of spectral emissivity of the sample surface and the infrared absorption of the sample cladding, coolant cylinder, and apparatus windows.

6. IRCON No. 1

IRCON No. 1 is a fast-response infrared pyrometer that also responds to radiation in the 2.0 to 2.6-μm range. It is capable of measuring surface temperatures between 400 and 1000°C over a single range with linear output. The instrument is an IRCON Model 6000 and is considered the most important of the pyrometers used in this experimental program. The temperature and instrument output relationship for IRCON No. 1 is

$$T(°C) = 400 + 60\,v_1, \tag{7}$$

where v_1 is the output in volts for this pyrometer. The possibility of using several pyrometers of this type, each sighted on a different surface location, has been considered.

7. IRCON No. 2

IRCON No. 2, an IRCON Model 2000, covers a middle range of temperature. The instrument is quite similar to IRCON No. 1, except that it responds to radiation in the 0.70 to 0.97-μm range and indicates temperatures from 900 to 1600°C. It has a linear output described by a relation of the form

$$T(°C) = 900 + 70\,v_2, \tag{8}$$

where v_2 is the output voltage of this instrument.

8. IRCON No. 3

IRCON No. 3 is only used for temperatures in the 1500-3000°C range. It is an IRCON Model 2000 and, like IRCON No. 2, has a spectral response in the 0.70 to 0.97-μm range. The output relation is of the form

$$T(°C) = 1500 + 150\,v_3 , \tag{9}$$

where v_3 is the output voltage of the instrument. It is expected that the temperature of the pellet stacks used in the program will not fall in this range except for centerline temperatures at high power levels.

9. Acoustic-emission Integrated Rms Signal

The acoustic-emission signal is provided by an Acoustic Emission Technology Corporation Model 3000 locator, which provides up to 100-dB gain for signals in the 175-kHz range and outputs these ac signals to other experimental devices. It provides a 0 to 5 V dc output that represents the rms value of the ac acoustic-emission signal. The cathode-ray tube (CRT) on the front of the locator displays a spatial distribution of events by means of threshold and coincidence circuitry.

For this program, the acoustic-emission rms signal is fed into a Johanson Model MA205-1 integrator. The output of this device is proportional to the integrated value of the input. Integration constants of 0.01, 0.1, 1.0, or 10.0 V-s may be selected. The purpose of this device is to provide an indication of the total accumulated crack damage to the pellet stack. An increase in the integrator output indicates the occurrence of fracture, and the rate of increase in the output can be related to the crack damage rate. The relatively long sampling intervals specified by EL (0.1, 1.0, and 10.0 min) will make it difficult to resolve individual fracture events from the output data. However, since the gain of the instrument will be fixed, it will be possible to determine the onset of fracture, damage rate, and total accumulated damage.

10. Acoustic-emission Event or Reset Count

The purpose of this data channel is to permit additional acoustic-emission information to be recorded. Although this channel is not presently used, it is believed that acoustic emission is the most fundamental experimental parameter to relate to cracking. Some of the basic acoustic-emission/fracture relationships are discussed below.

a. Accumulated Crack Damage. The total crack damage endured by a sample can be related to the total acoustic emission of that sample.

b. Crack Damage Rate. This is the time derivative of the above parameter.

c. Onset of Fracture. This experimental parameter can be measured by recording the time at which the integrated rms value of the ac acoustic-emission signal first changes.

d. Spatial Distribution of Cracks. The coincidence recording technique of the Model 3000 locator enables the device to display an axial distribution of fracture events in the sample. This distribution may be recorded at intervals by photographing the CRT or electrically scanning the memory of the locator.

e. Crack Count. This parameter is a measure of the total number of events rather than total acoustic energy associated with those events. The crack count may be obtained by counting the events displayed on the CRT of the locator, incorporating an electronic event counter, or monitoring the integrated rms value of the ac acoustic-emission signal at frequent intervals. For the last method to be effective, the experimental sampling rate should be less than the cycle time of the locator (5-50 ms, adjustable).

f. Temporal Distribution of Cracks. This parameter is simply an extension of the onset-of-fracture measurement. The importance of this parameter can be realized by observing the integrated rms signal. To assign a time of fracture to each event, however, it is necessary to sample at <5-ms intervals.

g. Crack Size. This information is obtained by observing the total acoustic emission during a single event. Prototypic tests have shown that total acoustic emission associated with a single crack may vary by several orders of magnitude. A good correlation can be found between crack size and acoustic emission if sampling rates are high enough.

h. Crack Type. It has been suggested that crack type (e.g., brittle/ductile) may be related to spectral distribution, pulse length, and other characteristics of the acoustic-emission signal. Argonne has shown that such spectral analysis of acoustic emission in DEH is difficult but possible. Therefore, it is not likely that this effort will be extended in the EPRI program.

To date, only the first four acoustic-emission/fracture relationships have been included in the current program. Additional information channels will be provided in the future as needed.

11. RETICON -- Diametral Measurement

The diameter of the pellet stack is continuously monitored with a Reticon Corporation RS859 Diameter Measurement System. The RS859 is an electrooptical system designed to provide high-resolution measurements [1.27×10^{-3} mm ($\pm 5 \times 10^{-5}$ in.)] of rod diameters by use of laser illumination. With this system, the shadow that results from laser illumination of the sample edge is magnified and projected on a linear array of photosensitive diodes. The number of illuminated diodes are counted and translated to a linear dimension. The system is quite sensitive to sample position in the laser beam [0.04 cm (±0.015 in.) tolerance]. In addition, the optical properties of the chamber windows, sample cladding, and coolant gas, which reduce the effective resolution to $\sim 1.27 \times 10^{-2}$ mm (5×10^{-4} in.), must be considered. When operating, the system displays four significant digits of the sample diameter. The last three digits are used to form an analog signal for the computer and multichannel recording systems. For example, a diametral measurement of 0.4321 in. would result in an analog output of 3.21 V. The high-order digit is ignored.

12. RETICON -- Axial Position

The recording of the axial position of the diametral measurement is to be implemented as soon as a translation stage for the RETICON is installed. It is anticipated that the linear measurement of this quantity will be obtained by means of an LVDT as described in the next section.

13. LVDT/Load Cell -- Axial Displacement/Load

Axial expansion or loading of the pellet stack is measured by means of a Daytronic Model 300D Transducer Amplifier Indicator. This instrument may be used with an LVDT to measure linear displacement or with a load cell to measure force. Since these measurements are usually made exclusively, current work has centered around the LVDT. The present equipment permits ±2.540, ±1.270, ±0.508, ±0.254, ±0.127, ±0.051, or ±0.0254 mm (±0.100, ±0.050, ±0.020, ±0.010, ±0.005, ±0.002, or ±0.001 in.), respectively, full-scale measurement. An output module has been modified to provide 0-10 V dc output over each full-scale range. Calibration of the transducer is provided by a standard 0.635-mm/revolution (0.025-in./revolution) micrometer.

14. Gas Flow Rate

Helium gas flow will be monitored by means of a 0 to 1132-liter/min (0-40 cfm) flowmeter. This meter provides an output signal that will be converted to 0-10 V dc full scale. The flowmeter has not yet been calibrated.

15. Water Content of the Gas Stream

The moisture content of the helium gas used to cool the pellet stack will be monitored with a Panametrics Model 2000 Hygrometer. The unit uses a gold-anodized aluminum oxide capacitive sensor to cover a dew-point range of +20 to -110°C. The manufacturer provides an individual calibration for each sensor probe. The calibrations show that each probe has a highly individual and nonlinear response. Therefore, the output of the instrument will be recorded in its raw form and converted to dew point later. Standard tables are used to equate dew point and H_2O concentration in the cover gas.

16. Oxygen Level in the Gas Stream

The oxygen level in the helium coolant gas is measured by a Thermox analyzer from Thermo-Lab Instruments, Inc. The instrument uses a zirconium oxide electrochemical cell to measure oxygen over three ranges when air is used as a reference gas. These ranges are 0.1-200,000, 0.1-10, and 1-100 ppm O_2. Calibration of this type of analyzer is obtained from the formula

$$E \sim AT \log (C_1/C_2) , \tag{10}$$

where E is the output of the cell, A is a scalar constant, T is the absolute temperature of the cell, C_1 is the O_2 concentration of the reference gas (air = 20.9% O_2), and C_2 is the O_2 concentration of the test gas.

E. Temperature Profiles *(C. R. Kennedy and J. C. Voglewede)*

Prototypic LWR surface and centerline temperatures as a function of nuclear power rating are shown in Fig. 9. A series of experiments has been performed to determine the degree of cooling necessary to alter the temperature profiles inherently found in direct electrically heated UO_2 pellets of the specified size and density to fit as closely as possible the prototypic surface and centerline temperatures.

In the preliminary tests, commercial UO_2 pellets 9.25 mm in diameter, 14.0 mm in length, and with a theoretical density (TD) of 94.5% were used in stacks of four pellets. These experiments closely approximate subsequent tests of experimentally fabricated pellet stacks of seven pellets with a length-to-diameter ratio equal to one. A total of 15 tests were conducted to determine the effects of gas flow rates and specimen-chamber geometry on the temperature gradients in the fuel pellets. Surface temperatures were measured by an infrared pyrometer and temperature gradients were calculated using the DEH steady-state temperature distribution (DEHSSTD) code, which is based on an analysis by Freund and Schikarski.[3]

The first test was conducted without an inner cylinder or "chimney" to channel the coolant gas around the surface of the pellets. A calculated temperature gradient of only 130°C was achieved with a helium flow rate of 680 liters/min and a surface temperature of 500°C. Subsequent experiments performed with chimneys that ranged from 24.0 to 11.7 mm in diameter resulted in a maximum calculated temperature gradient of only 310°C with the surface temperature at 600°C and a helium flow rate of 400 liters/min. However, prototypic temperature profiles have been generated for both clad and unclad pellet stacks through the use of a glass helix [inside diameter (ID) = 21.6 mm, outside diameter = 22.1 mm, length = 76.2 mm] inside a glass chimney (ID = 22.1 mm). The glass helix (replaced in later tests by a glass baffle as shown in Fig. 1) serves to break up the laminar gas flow into turbulent flow, thus increasing the cooling efficiency.

Using the chimney and baffle arrangement with unclad pellet stacks, center temperatures between 1500 and 2850°C (the melting point of UO_2) with surface temperatures of $\sim$500°C were achieved utilizing gas flows between 400 and 600 liters/min. When the 9.25-mm-diam pellets were surrounded by a 9.55-mm ID fused quartz tube to simulate a clad pellet stack, the effectiveness of the coolant gas was somewhat reduced. However, with the use of the chimney and helix, a center temperature of 1680°C and a surface temperature of 560°C were achieved with a gas flow rate of 600 liters/min.

Center temperatures in these tests were measured directly with an optical pyrometer sighted into a 1.2-mm-diam radial hole. This radial hole extended inward to intersect with a 1.2-mm-diam hole drilled along the axis of the pellet. Tests of the type described above are being used for final calibration of the DEHSSTD code over the range of anticipated variation.

F. Acoustic Emission *(D. S. Kupperman and C. R. Kennedy)*

The DEH apparatus has been used to generate thermal-gradient cracks for acoustic-emission studies. A previous study has demonstrated the feasibility of detecting acoustic-emission signals from thermal-gradient cracking without severely modifying the existent DEH apparatus.[4] In that study, stacks of four or five pellets were used, whereas supplementary experiments have now been conducted using single pellets. The results of both sets of experiments will be discussed. Two acoustic-emission monitors have been attached to the extensions of the upper and lower electrical feedthroughs of the DEH apparatus. This arrangement for detecting acoustic emissions could be improved significantly by placing waveguides attached to sensors into the heating chamber and connecting them directly to the electrodes. (The sensors would remain outside the chamber.) However, the purpose of the present study was to establish whether useful acoustic-emission information could be obtained without radical modification of the existent apparatus. Thus, this simple arrangement shown in Fig. 1 was used. It should be noted that the acoustic sensors are electrically insulated from the brass electrode extensions by a thin glass plate. This insulation is in addition to the electrical insulation provided by the acoustic-emission sensor element. A commercially available acoustic-emission locator and signal processer were used to sense the emissions from the pellet stack. The locator device (Fig. 3) detects and displays acoustic-emission events that occur between the two acoustic sensors. The sensors have a resonance frequency of 175 kHz. The system has the capability to divide the acoustic path between the transducers into 500 locations on the CRT. This system operates by calculating the difference in the arrival time of an acoustic wave at each of the two sensors. An event with a given time interval, which corresponds to a particular location, is then stored at that location on the CRT screen. In addition to acoustic-emission events detected and displayed, a continuous record of the rms value of the amplified and filtered acoustic-emission signal from the lower transducer is maintained.

The ends of the pellet stack are defined on the locator screen by striking the electrodes (to simulate acoustic events) above and below the pellet stack before placing the quartz cover over the system. For the present arrangement, the length of the five-pellet stack encompasses $\sim$200 of the 500 locations on the CRT screen. The gain setting was 100 dB for both transducers for all acoustic-emission data accumulation. The dead time between events sensed was 5 ms.

Although most data accumulated in these tests involve the counting of acoustic-emission events as a function of location, several runs have been made in which the acoustic-emission signal processor is used in the ringdown counting method of accumulating acoustic-emission data. In those cases, all acoustic emissions are received by the lower transducer. In the ringdown method, a count is made of the number of times the emission signal exceeds a preset amplitude threshold. Thus, as a result of the ringing of the transducer, one event may result in many counts. The ringdown method attributes more counts to larger signals as a result of the more extensive ringing. During all DEH tests, a continuous record of the pellet surface temperatures and the rms signal output of the locator was maintained.

Pellet surface temperatures were measured by means of an infrared optical pyrometer with a continuous output signal. A Honeywell CRT Visicorder was used for rms signal and temperature data acquisition.

Posttest examinations of the pellets heated to temperatures as high as 1700°C were conducted by polishing the ends of individual pellets and observing the crack patterns under a 16-power microscope.

1. Multiple-pellet Tests

As a result of the initiation and propagation of cracks in the pellets, bursts of elastic energy are transmitted through the pellet stack and electrodes and are ultimately received by the acoustic-emission sensors. These events are detected electronically as damped sinusoidal waves and can be observed on an oscilloscope using the ac output on the acoustic-emission equipment. Since surface waves attenuate less than shear and longitudinal waves, it is probable that the acoustic sensors are responding to surface waves. Some of the acoustic waves travel directly to the transducer, and others are reflected and reach the transducer later. Premature triggering by the reflected waves is minimized by the dead time between the recording of events. The cracks are assumed to propagate in a stepwise fashion and at a relatively slow rate. Thus, crack growth along the pellet-stack axis should be observed as a series of acoustic-emission events at sequential locations on the CRT screen. Radial crack growth should be observed as an event accumulation near one of the locations of the acoustic-emission locator screen. Simultaneous crack generation might lead to spurious results. Since the total number of events recorded is not high (only strong emissions are recorded), the problem of distorted event counting is somewhat minimized. The resolution capability of the acoustic-emission system imposes the most severe limitation on the location of the source of acoustic emission in a pellet stack.

Figure 10 shows the temperature and acoustic-emission count rate versus time for a pellet stack heated to ∿1400°C in 150 s. The initiation of significant acoustic emission, and thus cracking, appears to occur at a surface temperature of ∿600°C. Although the temperature in this test is not accurately known below 900°C, subsequent experiments with improved temperature-monitoring techniques support the result that acoustic emission initiates at ∿600°C in these particular tests. During the steady temperature phase of the test, acoustic-emission activity is quite low. After turning the current off for rapid cooling, a relatively intense but short period of acoustic-emission activity is observed. This test produces useful information on acoustic-emission activity and crack initiation but does not provide information concerning the relative location of the source of acoustic-emission activity.

When the two-transducer method is used, the relative location of acoustic-emission events can be obtained. Figure 11 shows the histogram for acoustic-emission events accumulated during heating and cooling phases of a four-pellet stack. Each pellet represents ∿40 channels on the locator screen. Events have been counted in groups of ∿20 channels and have been plotted on the resultant histogram. Thus, each pellet is represented by two bars. Figure 11 indicates that the acoustic-emission activity is indeed

concentrated within the pellet-stack limits, as determined by the calibration procedure, and the activity is quite uniform across the pellets. On cooling, the activity is slightly higher toward the ends of the stack. The posttest visual examination of the four pellets showed a uniform distribution of cracks, which supports the results of the acoustic-emission data. Figure 12 shows an acoustic-emission experiment with a five-pellet UO_2 stack that indicates significantly more acoustic emissions, and thus cracking, in the upper pellets than in the lower portion of the stack. Posttest examination again supported the results of the acoustic-emission data. The upper pellet disintegrated upon removal from the DEH apparatus, but the remaining pellets were intact and were, in general, of uniform crack density. The resolution available to locate the source of acoustic emission is not as accurate as might be suggested by the number of memory channels available for storing events at different locations. This is a result of the limitations of the acoustic-emission system for detecting the short distances in these tests and the dispersion and scattering of acoustic waves.

Through observation of the time sequence of acoustic emissions as a function of location on cooling, it appears that emissions originate at the ends of the pellet stack and progress toward the center. This pattern follows the expected behavior of cooling along the pellet stack, since the end pellets are in contact with the water-cooled electrodes and therefore lose heat faster than the center pellets. As a result of the initial large temperature gradient at the electrodes, acoustic emissions are generated near the ends of the stack. Thus, when the effects of temperature cycles on cracking are analyzed, it is important to discard data obtained from the two end pellets in the stack since their behavior is somewhat anomalous.

Acoustic-emission monitoring of the fuel pellets would be particularly useful if the extent of cracking in a given pellet was associated with the number of acoustic-emission events. In fact, for pellets with similar types of cracking patterns, a reasonable correlation can be made between the total number of acoustic-emission events and cracking. The extent of cracking is established by measuring the total length of cracks visible from both ends of the pellet after posttest polishing and examination. Since photographs of the ends of the pellets fail to reveal the axial cracks that sometimes occur, the correlation of acoustic emission with crack density has been confined to pellets with similar cracking, i.e., primarily radial cracking. The results for 23 pellets are shown in Fig. 13, in which the total number of acoustic-emission events for a given pellet has been plotted versus the average total crack length measured at the end of the pellet. The variation in crack density is the result of changing the maximum temperature and heating rate of the pellets. The correlation between total crack length and total acoustic-emission events for a pellet is reasonable and supports the suggestion that acoustic emission can be useful in monitoring thermal-gradient cracking in UO_2.

The acoustic-emission activity observed during a DEH experiment is also indicative of the oxygen content in the gas environment that surrounds the heated pellets. Improper purging of the system with helium gas results in an undesirable amount of residual oxygen. The presence of oxygen leads to excessive cracking and flaking on heating and, as a result, a significant

increase in acoustic-emission activity (as much as 100 times that observed when heating in an inert environment).

As previously mentioned, the rms signal output of one of the transducers is continually monitored during a DEH experiment. This signal provides information similar to that obtained by the ringdown counting method (Fig. 10). A chart of the rms voltage as a function of time is shown in Fig. 14. Superimposed on this chart is a trace of temperature versus time. The acoustic-emission activity is greatest during steep temperature gradients, as expected, and is intense during cooldown. This signal monitoring provides useful supplementary information to the event counting as a function of location, since it gives a permanent indication of the total acoustic-emission activity versus time and temperature.

The recording of acoustic-emission activity has also been shown to be useful in monitoring thermal-shock cracking during power transient tests.[2] In these tests, the apparatus is used to simulate in-reactor loss-of-flow (LOF) conditions and verify escape-path mechanisms. These tests have been run in a modified DEH apparatus using the same transducer configuration as that shown in Fig. 1. Figure 15 shows acoustic emissions during a power transient via the rms signal from the lower transducer of Fig. 1. Significant activity is present during the intervals of large temperature gradients (heating and cooling). The loss of acoustic-emission signal indicates the onset of liquification of the pellets. These results suggest that cracking occurs during rapid power transients prior to gross melting. Again, acoustic-emission monitoring provides information that cannot be obtained by other methods.

2. Single-pellet Tests

The multiple-pellet tests have suggested that complex and extensive cracking patterns in UO_2 can to some extent be characterized by the amount of acoustic energy generated during crack formation. To understand more thoroughly the correlation between acoustic emission and cracking, single-pellet tests were run. In these tests, the pellet was heated slowly until the onset of acoustic-emission signals and was then cooled. As a result, a minimum number of cracks were generated. The acoustic-emission signals are monitored and processed via the rms voltage-output circuit and ringdown counting method.

The strength of the acoustic-emission signal generated by the initiation and propagation of a crack should be related to the total surface area of the resultant crack. Ten pellets were heated in the DEH apparatus, and the number of cracks varied considerably. All 10 pellets were monitored via the rms circuit, and four of these were also monitored using the ringdown technique. After the tests were completed, a fluorescent dye penetrant was used with the expectation that the dye would fill the cracks and coat the crack surfaces. After a 25-h soaking period, the pellets were heated to $\sim$100°C to dry the penetrant. This is necessary to prevent the spread of the penetrant upon opening the pellets. The pellets were then broken to reveal the penetrant and obtain an estimate of crack surface area. The uncertainties associated with this technique are reasonably large. The penetrant may not

have covered all cracked surfaces, the destructive examination may not have revealed all surfaces covered by the penetrant, and accurate determination of the total surface area covered by the dye penetrant is quite difficult. Nevertheless, despite the complexity of the crack patterns and the problems associated with estimating the area of these irregular cracks, a clear trend is evident when data on the crack area versus rms signal are presented. Figure 16 shows the results of these experiments. The crack surface-area range is from 8 to 50 mm^2, whereas the total rms output range extends from 0.36 to 2.67 V. A least-squares linear fit to the data is shown. The coefficient of correlation is 0.87.

In Figure 17, the total rms signal from acoustic emissions is plotted as a function of total crack length. This length parameter is the total length of a crack visible at both ends of the pellet after a completed run in the DEH apparatus. A reasonable correlation exists between crack length and rms signal. Although a more accurate representation of the crack should be obtained by measuring the crack surface, the problems inherent in determining the crack surface area appear to reduce the correlation between area and acoustic-emission signal to the extent that it is comparable to the correlation between crack length and rms signal.

Ringdown counting was monitored for four single-pellet tests. The summation of counts has been plotted versus total crack length in Fig. 18 and total surface area in Fig. 19. Both figures show the same general trend, with a threshold for counting evident. This is understandable in view of the fact that ringdown counting has a preset threshold level below which no count accumulation occurs. Thus, no counts are accumulated for pellets with limited cracking, although an rms signal is observable. For pellets with larger cracks and stronger signals, the threshold is exceeded and counts are accumulated. The data suggest that, for severe cracking, count accumulation may result in better correlation with pellet damage than rms signals. More work is needed to accurately assess the possible correlations between acoustic emission and thermal-gradient cracking.

G. Pellet-cladding Mechanical Interaction Strain Measurements *(W. A. Ellingson)*

1. Strain-gauge Application

Electrical-resistance strain gauges have become widely accepted as a means of measuring local strain on specimens. Operation of electrical-resistance strain gauges at temperatures in the range 400-1000°C, however, introduces several problems.

A strain gauge attached to a specimen will show a strain indication if the gauge installation is heated. This purely temperature-induced resistance change will be recorded as strain and is referred to as apparent strain. Apparent strain is caused by two concurrent and algebraically additive effects in the strain-gauge installation. First, the electrical resistivity of the grid conductor is temperature dependent, and any resistance change with temperature due to this effect appears as strain on a strain indicator. The second contribution to apparent strain is caused by the differential thermal expansion between the grid conductor and the specimen or substrate material

to which the gauge is bonded. With temperature change, the substrate expands or contracts; and, since the strain gauge is firmly bonded to the substrate, the gauge grid is forced to undergo the same expansion or contraction. To the extent that the thermal expansion coefficient of the grid differs from that of the substrate, the grid is mechanically strained when it conforms to the free expansion or contraction of the substrate. Since the grid is, by design, strain sensitive, the resultant resistance change appears on the strain indicator as strain in the substrate.

The net temperature-induced apparent strain can be expressed as the sum of the resistivity and differential expansion effects:

$$\varepsilon_{APP(G/S)} = \left[\frac{\beta_G}{F} + (\alpha_S - \alpha_G)\right]\Delta T \ , \tag{11}$$

where, in consistent units, $\varepsilon_{APP(G/S)}$ is the apparent strain of grid material G on substrate material S, β_G is the thermal coefficient of resistance of the grid conductor, F is the gauge factor, $(\alpha_S - \alpha_G)$ is the difference in thermal expansion coefficient of substrate and grid, respectively, and ΔT is the temperature change from arbitrary initial reference temperature. It should not be assumed from the form of Eq. 11 that the apparent strain is linear with temperature, because all of the coefficients within the brackets are themselves functions of temperature. The equation clearly demonstrates, however, that the apparent strain exhibited with temperature change depends not only upon the nature of the strain gauge but also upon the material to which the gauge is bonded. Because of this, apparent strain data are meaningful only when they refer to a particular grid alloy bonded to a specified substrate material.

The substrate material in this case is fused silica, and the initial gauges being evaluated are 6 mm long, free filament, Baldwin-Lima-Hamilton Type HT-1212-2A — laid with CER-1200 activator. Application of the gauge to the fused silica requires a surface preparation that enhances bonding between the CER-1200 and silica. Several experiments to evaluate surface preparations were performed. The results indicate that use of a fine diamond-grit blast would yield good adherence. The adherence was checked by mechanical load and visual inspection under magnification. Critical to the application is the employment of a thin initial layer of CER-1200 for the free-filament substrate.

Figure 20 shows the apparent strain measured during the third and fourth thermal cycle of an instrumented cylinder heated in a furnace. Note that although the magnitude of the maximum apparent strain is quite high, up to 3800 $\mu\varepsilon$ (where ε is strain), the repeatability for the two runs is within 50 $\mu\varepsilon$ (above 250°C), and, thus, the error attributable to apparent strain seems acceptable in the temperature range of interest. Figure 21 shows the instrumented fused silica cylinder from which the apparent strains shown in Fig. 20 were determined. The thermocouple used to monitor the strain-gauge installation temperature was placed on the same substrate coating as the free-filament strain gauge. Figure 22 shows the overall apparatus used in this initial study. The strain indicator has provision for continuous strain monitoring, and both temperature and strain were continuously recorded on the strip-chart recorder during these investigations.

2. Stress Analysis

A thin-wall cylinder has a wall thickness such that the assumption of constant stress across the wall results in negligible error. Cylinders with internal diameter-to-thickness ratios >10 are usually considered thin wall. For the PCMI studies, the wall thickness of the fused silica cylinder is ∿1 mm and the internal ID ∿9.5 mm. Thus, the ratio is 9.5 and the cylinder can be considered thin wall. All initial analysis will assume plane stress.

H. Pellet Fabrication *(C. R. Kennedy)*

Pellets have been fabricated by conventional pressing and sintering techniques. The UO_2 powder was ball milled for 48 h, dried, passed through a 60-mesh sieve, and then pressed in a 12.7-mm (0.5 in.) diam die at 1.03×10^2 MN/m^2 (15,000 psi). The pressed pellets were then sintered in lots of 30 at a maximum temperature of 1680°C (3056°F) for 1 h in a flowing hydrogen gas atmosphere. The resultant sintered pellets were 10.03 mm (0.395 in.) in diameter and had an average TD of 96.2% (10.55 g/cm^3 actual density) as measured by the water-immersion technique. The 95% confidence limits for the variation of the density of 15 pellets (five each from three different firings) was ±0.3% TD, with the extreme values being 96.7 and 95.9% TD. The oxygen-to-metal (O/M) ratio was 2.000 ± 0.001. The average grain size, as measured by a linear intercept technique and corrected to a "true grain size" by a multiplication factor of 1.57, is 7.2 μm with 95% confidence limits of ±0.6 μm.

Figure 23 shows the pore size and shape of a polished sintered pellet. Pores up to 0.15 mm (5.5×10^{-3} in.) in diameter have been observed. Figure 24 shows the grain size and shape. Note the occurrence of both intergranular and intragranular porosity. A spectrochemical analysis has been performed on a sintered UO_2 pellet and the results are listed in Table VIII. A quantitative pore-size analysis will be conducted to complete the characterization of the pellets.

I. Fracture-mechanics Specimen Fabrication *(C. R. Kennedy)*

Initial problems encountered in fabrication of sintered plates have been solved. Laminations occurred when the UO_2 powder was pressed at 1.03×10^2 MN/m^2 (15,000 psi) in a 76.2 × 38.1-mm (3 × 1½ in.) die to yield a plate 2 mm (0.079 in.) thick. In addition, severe cracking was evident after sintering at 1680°C (3056°F) for 1 h in a flowing hydrogen gas atmosphere. Therefore, a series of plates were prepared that contained 2, 4, or 6% of either stearic acid or Carbowax as a binder. These binders were introduced by dissolving them in methyl alcohol, mixing with the UO_2 powder, and drying thoroughly while stirring to minimize segregation. The mixtures were then passed through a 30-mesh sieve and pressed. The 94% UO_2-6% Carbowax plates were free of laminations in the green state and did not warp when fired. However, each specimen contained a number of small cracks around the edges. This problem was minimized by moistening the dry UO_2-Carbowax mixture with 75 drops of alcohol just prior to pressing. Seventeen sintered plates have been sent to A. G. Evans at RI for fracture-mechanics testing.

TABLE VIII. Spectrochemical Analysis of a Sintered UO_2 Pellet (parts per million)

Element	Concentration	Element	Concentration
Ag	<1	Nb	<10
Al	40	Nd	<10
As	<20	Ni	25
B	0.2	P	<50
Ba	<2	Pb	<1
Be	0.1	Rb	<10
Bi	<1	Sb	<5
Ca	30	Sc	<1
Cd	<5	Si	10
Ce	<10	Sm	<10
Co	<5	Sn	<2
Cr	8	Sr	0.1
Cs	<50	Ta	<10
Fe	10?	Th	<10
K	<50	Ti	5
Li	<0.1	V	<5
Mg	1.5	W	<10
Mn	0.7	Zn	<20
Na	30	Zr	<2

The average immersion density of the 17 sintered plates is 10.27 g/cm^3, which is 93.7% TD. The 95% confidence limits for the variability of the density of these plates is ±0.2% TD, with the extreme values being 94.3 and 93.3% TD. The O/M ratio is 2.000 ± 0.001. The average grain size (Fig. 25), as measured by a linear intercept technique and corrected to a "true grain size" by a multiplication factor of 1.57, is 6.7 μm, with 95% confidence limits of ±0.5 μm.

Figure 26a is a photomicrograph of the microstructure of a sintered plate obtained perpendicular to the direction of pressing, whereas Fig. 26b was obtained parallel to the direction of pressing. Examination of these photomicrographs reveals a wide range of pore sizes, including a number of large pores [up to 0.4 mm (0.157 in.)] that are slightly lenticular, with the minor axis parallel to the pressing direction. The occurrence of these pores indicates imperfect binder distribution, but they are not expected to influence the fracture-mechanics determinations.

J. Fracture Mechanics of Nuclear Fuels *(Subcontracted to Rockwell International)*

1. Introduction

The length and location of macrocracks in a nuclear fuel pellet, at any time t in its life cycle, are determined by the state of stress present in the pellet and the stress-intensity factor, which are crack-growth characteristics of the material. For an integral body, the stress can be determined by numerical analysis; but the crack-growth characteristics of the material involve parameters the values of which must be determined by experiment. The present study is concerned with the determination of these values for conventional sintered UO_2.

At elevated temperatures in a neutral environment cracks can either propagate by deformation-assisted crack growth[5] or recede by surface diffusion.[6-8] The tendency for growth or recession is determined by the temperature and the stress-intensity factor, K (Fig. 27).[5] At a critical stress-intensity factor, K_c, crack propagation is essentially catastrophic; but as K decreases, the crack-propagation rate (da/dt) diminishes and reaches a negligible value below K_g. Conversely, at low K, the crack recedes; but the healing rate (-da/dt) diminishes as the time or stress-intensity factor increases, reaching a negligible value above K_h, as indicated in Fig. 27. The region between K_g and K_h is thus a regime of crack metastability. The objective of the present study is to evaluate the stress-intensity factor terms K_c, K_g, and K_h as a function of temperature and then to deduce their implications for crack stability in fuel pellets.

2. Experimental Procedure *(A. G. Evans, Rockwell International)*

The crack-propagation and crack-healing studies utilize the double-torsion specimen configuration.[9] As-fabricated plates of sintered UO_2 (0.002 m thick) were cut to size (0.05 × 0.02 m) and side grooved along the length direction (to a depth of 0.001 m), and a chevron edge notch[9] (0.01 m in length) was introduced at one end. The samples were immersed in water and precracked from the edge notch by loading in the double-torsion test fixture

at a constant displacement rate of 10^{-6} ms^{-1}. The formation of the precracks was detected by attaching an acoustic-emission transducer to the upper surface of the test sample.[9]

The precracked samples were then tested in an Instron machine using a silicon carbide fixture.[9] The tests were performed either at room temperature in a moist environment or at elevated temperatures (800 to 1400°C) in vacuum. Crack-propagation tests were conducted under constant displacement rate or constant displacement conditions while the load was monitored as a function of time.[5,9] Acoustic emission was also monitored during the room-temperature tests. Crack-recession tests were conducted under constant, or zero, load conditions.[5,9] Crack lengths were measured at the beginning and end of each test using a fluorescent dye penetrant to indicate the position of the crack.

Several samples used for the crack-healing studies were mechanically polished after the test and inspected in the optical microscope to determine the crack-healing morphology.

3. Results *(A. G. Evans, Rockwell International)*

a. Crack Propagation. Critical stress-intensity factors for this material were first obtained, as a function of temperature, by loading the samples at the maximum feasible rate. The data obtained are plotted in Fig. 28. The stress-intensity factors are consistent with data obtained by Evans and Davidge[10] and indicate a slight increase in K_c at temperatures $\gtrsim$1000°C.

Moisture-dependent slow crack propagation (stress corrosion) was detected at room temperature, as indicated by the crack-propagation results summarized in Fig. 29. However, the stress-corrosion susceptibility (determined by the slope) appears to be minimal.

Slow crack propagation has also been detected at temperatures $\gtrsim$1000°C. Some typical data are plotted in Fig. 29. Again the slow crack growth susceptibility is minimal, at least at temperatures up to 1400°C. The limited slow crack growth at these temperatures has been checked by examining the stress-rate dependence of the fracture strength of notched flexure bars[11] (Fig. 30). The relative insensitivity of the strength to the stress rate is consistent with a narrow range of slow crack growth.

b. Crack Healing. The crack-healing kinetics have been investigated at 1400°C. First, the crack-morphology observations indicated a zone of partial healing ahead of the primary crack, which is consistent with observations on other polycrystalline ceramics.[8] The partially healed zone consisted of secondary cracks several grain diameters in length, separated by void and cylinder arrays. The recession of the primary crack front at the surface was used as a measure of the crack healing. The changes in crack length obtained thereby are plotted as a function of time in Fig. 31. The crack-healing rate, determined in this manner, is time and stress-intensity factor dependent and can be expressed in functional form by the relation

$$-\frac{da}{dt} = b(tK^3)^{-0.4}, \qquad (12)$$

where b is a constant and t is time.

c. Crack Repropagation. The repropagation of partially healed cracks was studied at room temperature in dry nitrogen gas (which averts slow crack growth) to determine whether the crack-propagation behavior in the partially healed material differs from that in the virgin material. This was accomplished by monitoring acoustic emission to indicate the onset of crack propagation and making intermittent compliance measurements to determine the crack length.[9] Then, from the crack-length dependence of the load, the change in stress-intensity factor, K_c', with crack extension could be deduced. The results are plotted in Fig. 32. Also, shown for reference is the extent of the partially healed zone. It is apparent that initial propagation occurs at a low critical stress-intensity factor but a crack-propagation resistance equivalent to that for the virgin material is quickly reestablished, well within the partially healed zone. A functional relation between K_c' and K_c is

$$\frac{K_c'}{K_c} = \left(\frac{2}{\pi}\right) \tan^{-1}\left(\frac{\Delta a}{a^*}\right), \tag{13}$$

where Δa is the change in crack length and a^* is a constant equal to $\sim$500 μm.

4. Discussion

Crack Motion. The minimal slow crack growth in the virgin material and the small zone of degradation ahead of partially healed cracks indicate that the crack-propagation condition for this material is adequately characterized, for most purposes, by the critical stress-intensity factor K_c, which is obtained from Fig. 28. Furthermore, the strong dependence of the crack-recession rate on the stress-intensity factor, and to a lesser extent on time (Fig. 31), indicates that little crack recession is likely to occur during the expected lifetime of a typical fuel pellet, provided the stress-intensity factor is maintained $\gtrsim$0.4 $MNm^{-3/2}$. However, if K is allowed to decrease below $\sim$0.2 $MNm^{-3/2}$, then significant crack healing can occur, increasing rapidly as K is reduced.

REFERENCES

1. B. J. Wrona, J. T. A. Roberts, E. Johanson, and W. D. Tuohig, "First Report on Apparatus to Simulate In-Reactor Transient Heating Conditions in Oxide Fuel Columns," Nucl. Tech. 20, 114 (1973).

2. B. J. Wrona and E. Johanson, "Development of Direct-Electrical-Heating Apparatus to Study the Response of Nuclear Fuels to Applied Transients," Nucl. Tech. 29, 433 (1976).

3. D. Freund and W. Schikarski, "The Direct Electrically Heated UO_2 Fuel Rod," EURATOM Fast Neutron Reactor, EURFNR-775 (English translation of KFK-1031), Karlsruhe Research Center (1970).

4. C. R. Kennedy, D. S. Kupperman, and B. J. Wrona, "Acoustic Emission from Thermal-Gradient Cracks in UO_2," Mater. Eval. 34, 91-96 (1976).

5. A. G. Evans, "High-Temperature Slow Crack Growth in Ceramic Materials," in *Ceramics for High Performance Applications*, J. J. Burke, A. E. Gorum, and R. N. Katz, eds., Brook Hill Publ. Corp., Chestnut Hill, Mass., 1974, p. 373.

6. J. T. A. Roberts and B. J. Wrona, "Crack Healing in UO_2," J. Am. Ceram. Soc. 56, 297-299 (1973).

7. G. Bandyopadhyay and J. T. A. Roberts, "Crack Healing and Strength Recovery in UO_2," J. Am. Ceram. Soc. 59(9-10), 415-419 (1976).

8. A. G. Evans and E. Charles, "Strength Recovery by Diffusive Crack Healing," to be published.

9. A. G. Evans, "Fracture Mechanics Determinations," in *Fracture Mechanics of Ceramics*, R. C. Bradt, D. P. H. Hasselman, and F. F. Lange, eds., Plenum Press, New York, 1974, p. 17.

10. A. G. Evans and R. W. Davidge, "The Strength and Fracture of Stoichiometric Polycrystalline UO_2," J. Nucl. Mater. 33, 249 (1969).

11. A. G. Evans, "Slow Crack Growth in Brittle Materials under Dynamic Loading Conditions, Intl. J. Fract. 10, 251 (1974).

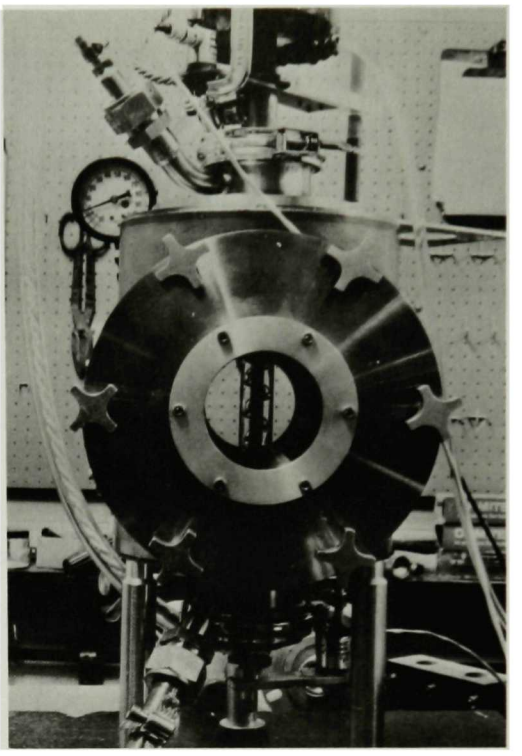

Fig. 1. The DEH Specimen Chamber.
Neg. No. MSD-63469.

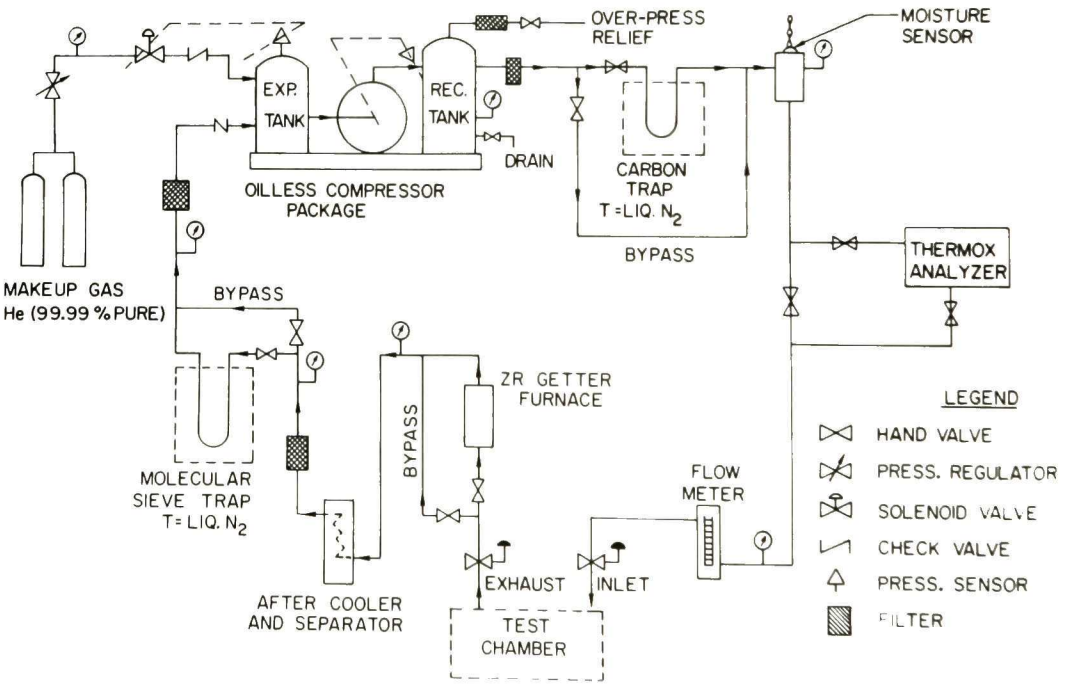

Fig. 2. Helium Recirculating System for the DEH Apparatus.
T is temperature. Neg. No. MSD-62473.

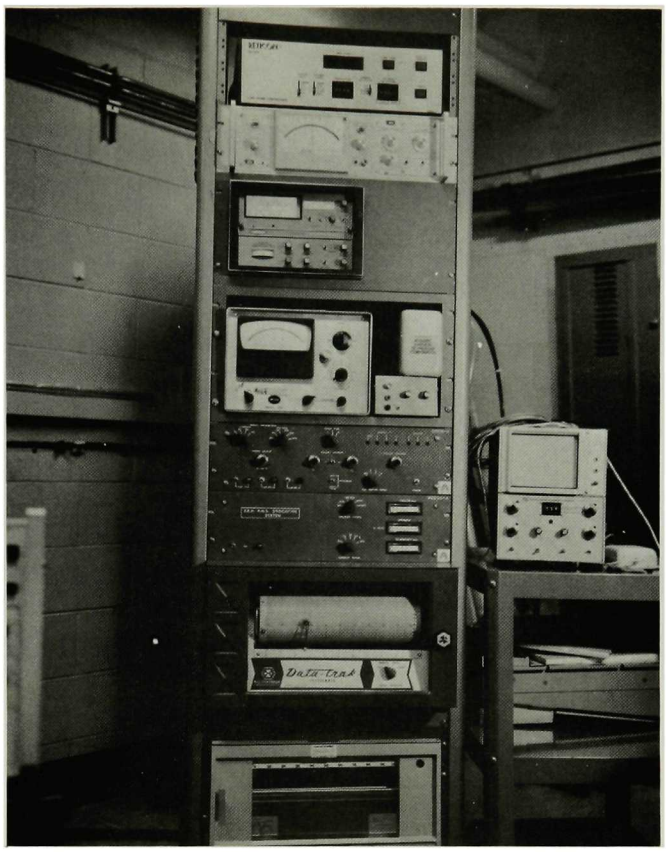

Fig. 3. The DEH Instrumentation Panel.
ANL Neg. No. 306-76-282.

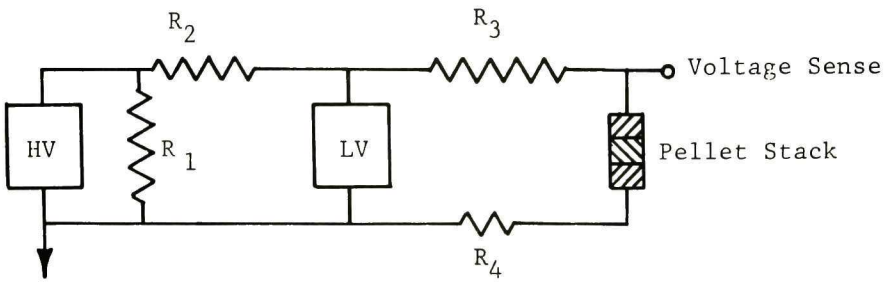

HV = High-voltage, low-current power supply, 2500 V, 10 A.

LV = Low-voltage, high-current power supply, 300 V, 300 A.

R_1 = Ballast resistor, 2000 Ω, 2500 W.

R_2 = High-voltage limit resistor, 625 Ω, 8000 W.

R_3 = High-current limit resistor, 0.4 Ω, 5000 W.

R_4 = Current shunt, 50 mV, 100 A.

Fig. 4. Schematic of Power Supply. Neg. No. MSD-63471.

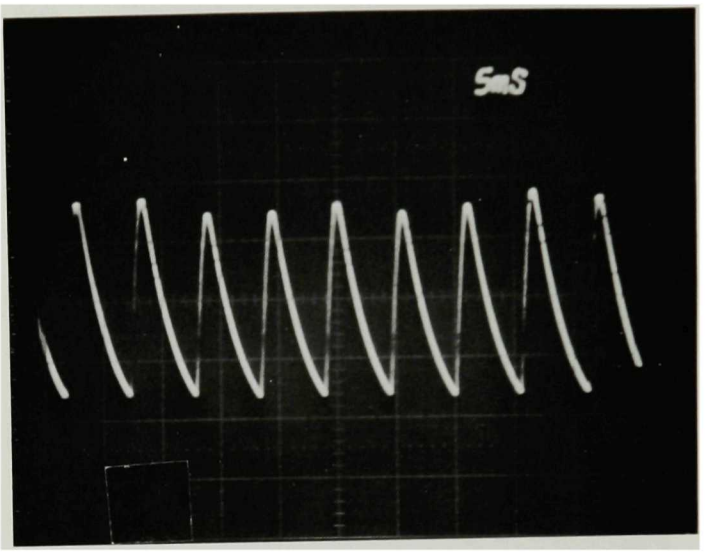

Fig. 5. Raw Voltage Signal across Pellet Stack.
ANL Neg. No. 306-76-283.

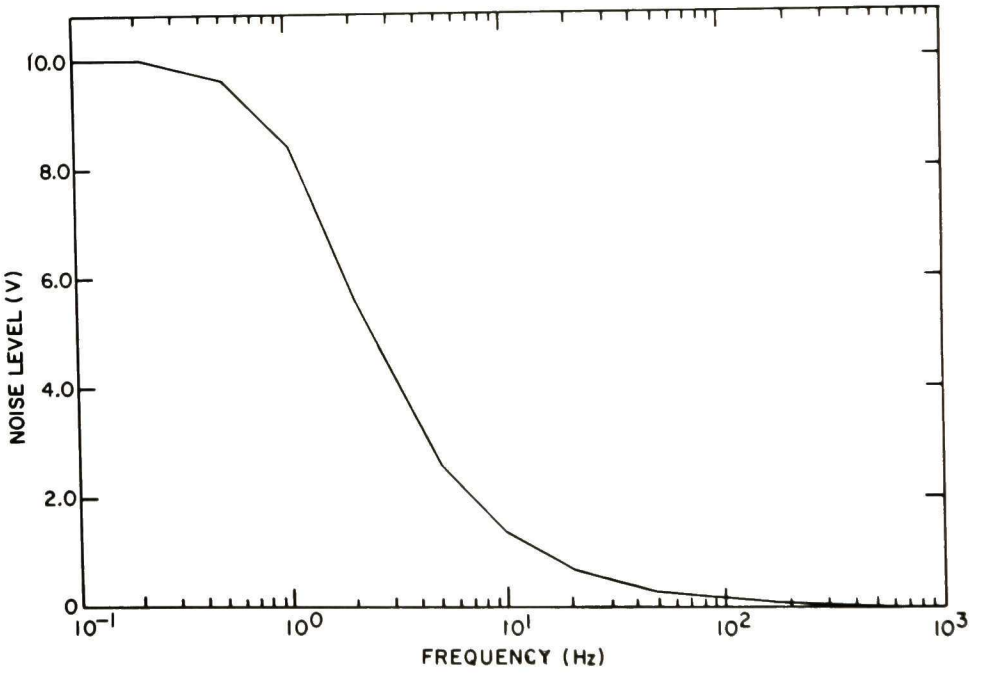

Fig. 6. Noise Level of Rms Converter as a Function of Input Signal Frequency. Neg. No. MSD-63472.

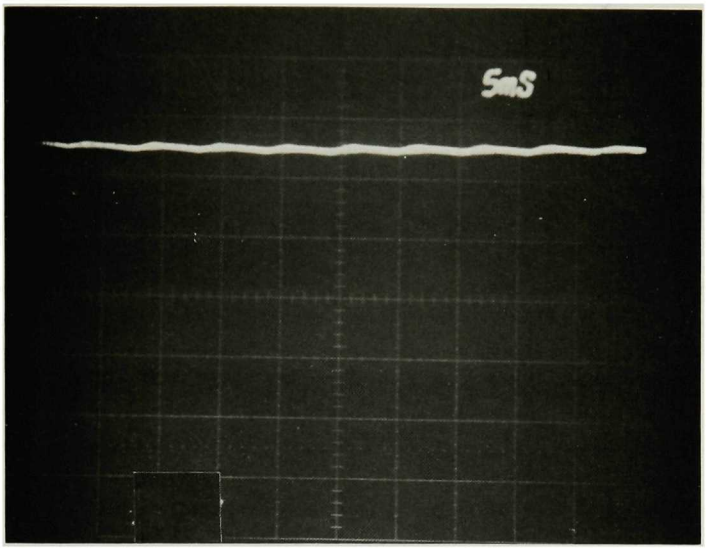

Fig. 7. Rms Output Signal. ANL Neg. No. 306-76-284.

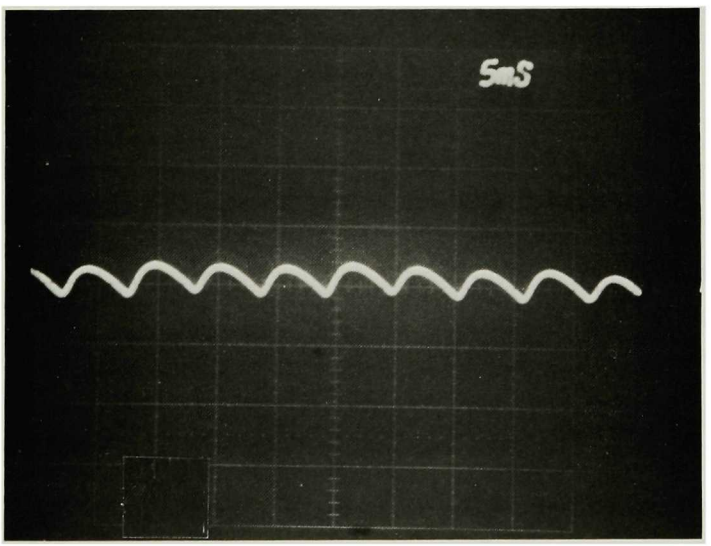

Fig. 8. Ripple on Rms Output Signal. ANL Neg. No. 306-76-285.

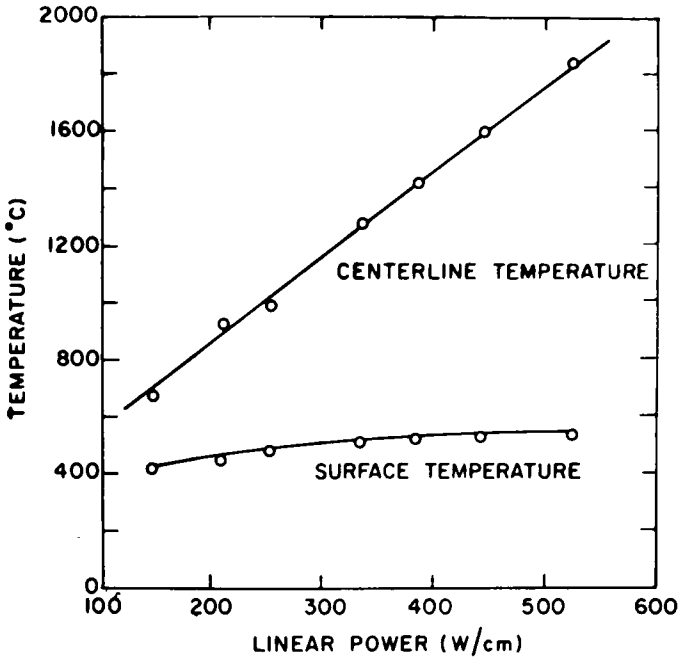

Fig. 9. Prototypic LWR Surface and Centerline Temperatures as a Function of Nuclear Power Rating. Neg. No. MSD-63498.

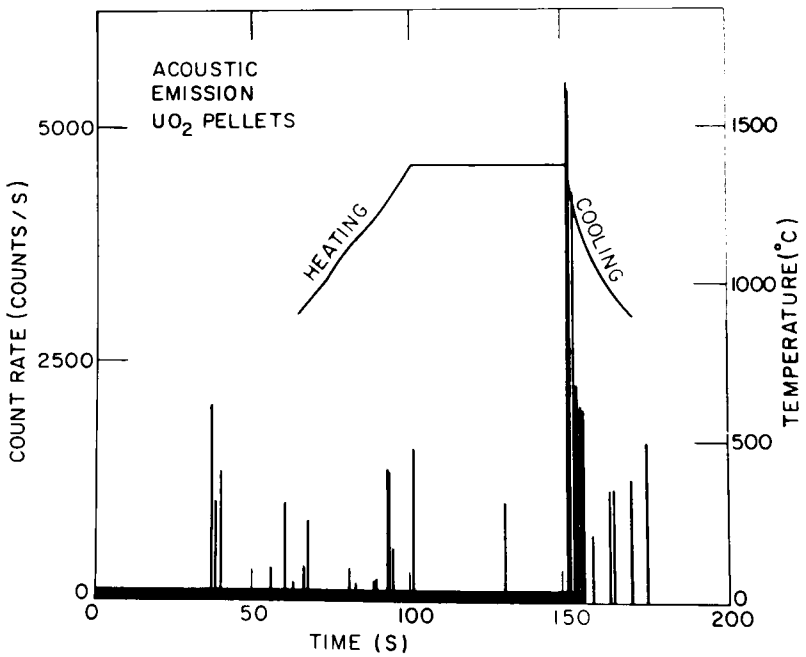

Fig. 10. Acoustic-emission Count Rate vs Time and Temperature of the Pellet Surface as a Function of Time for a Four-pellet Stack Heated to 1400°C in 150 s. Acoustic emissions are received by the lower transducer shown in Fig. 1. Neg. No. MSD-61540.

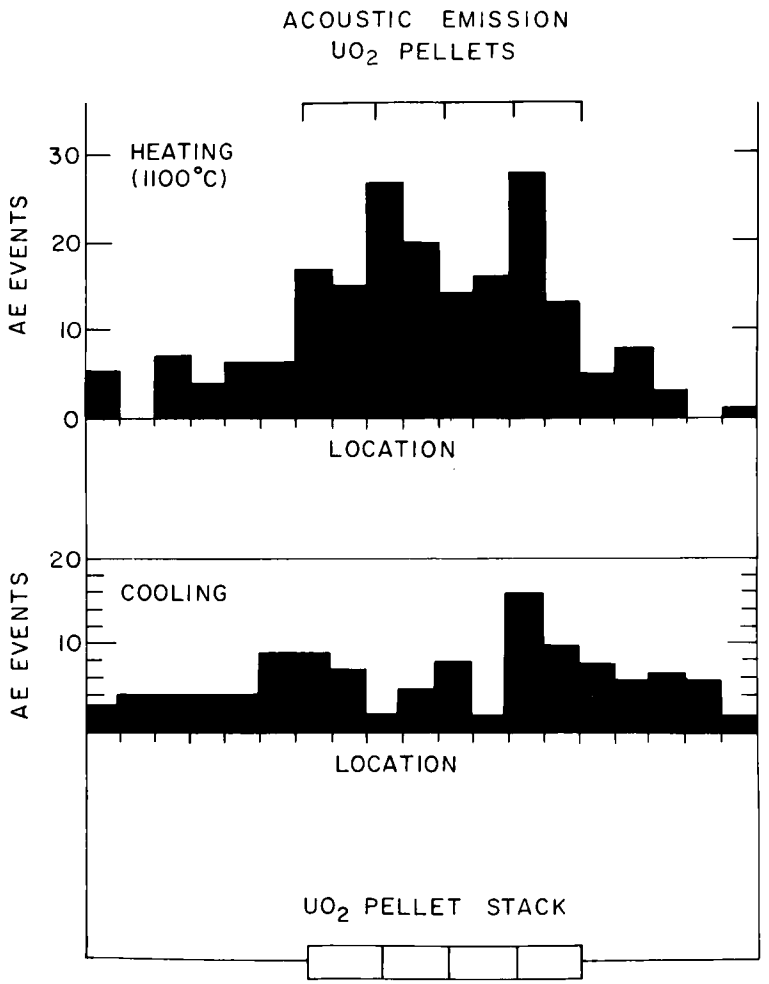

Fig. 11. Acoustic-emission Events as a Function of Location for a Four-pellet UO_2 Stack. Each vertical bar represents the total number of events and encompasses ∿20 memory channels of the acoustic-emission locator. Each pellet is represented by two bars in the histogram. Neg. No. MSD-60854.

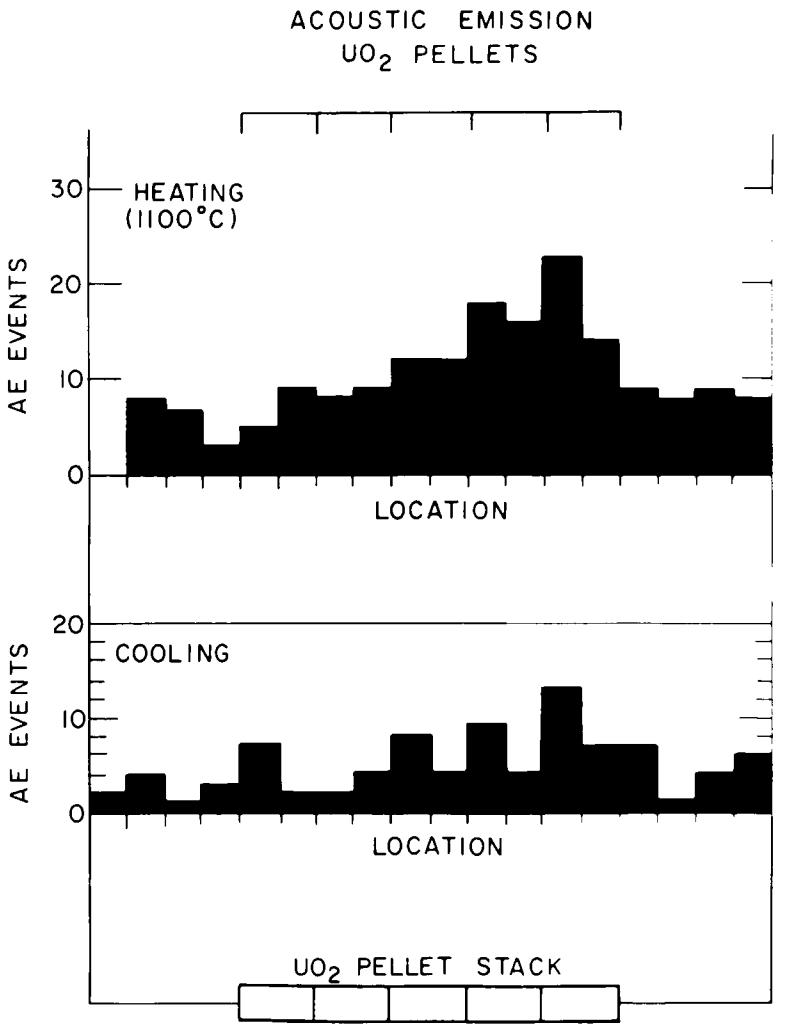

Fig. 12. Acoustic-emission Events as a Function of Location for a Five-pellet UO_2 Stack. Neg. No. MSD-60853.

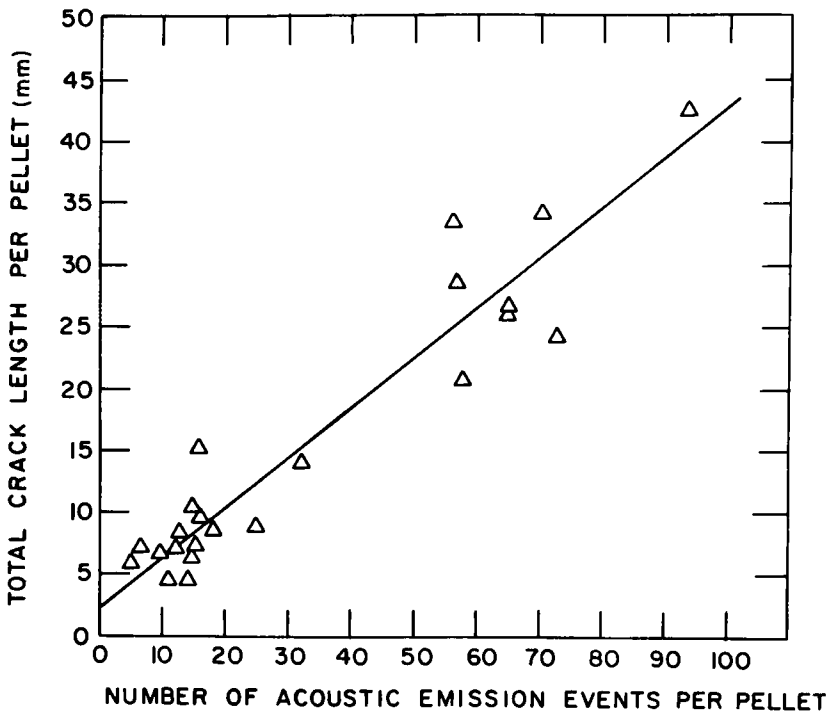

Fig. 13. Total Number of Acoustic Emissions per Pellet vs Total Crack Length Measured from the Ends of the Pellets in Posttest Examination. Neg. No. MSD-63441.

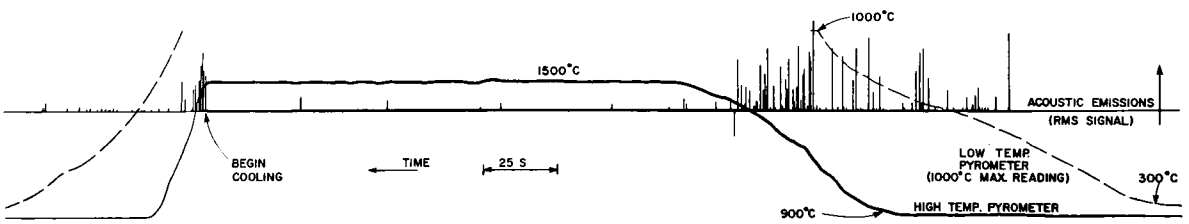

Fig. 14. Rms Signal Output of the Acoustic-emission Locator vs Time and Pellet Surface Temperature vs Time for a Five-pellet Stack. Neg. No. MSD-61538.

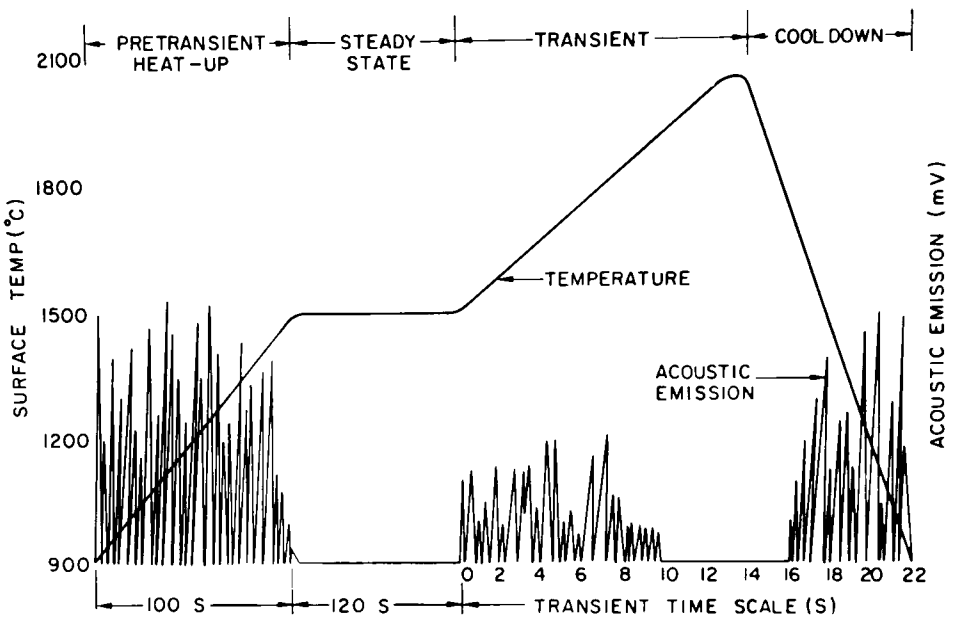

Fig. 15. Acoustic-emission Activity via Rms Signal Output during a Power Transient in a Five-pellet Stack. Neg. No. MSD-60955.

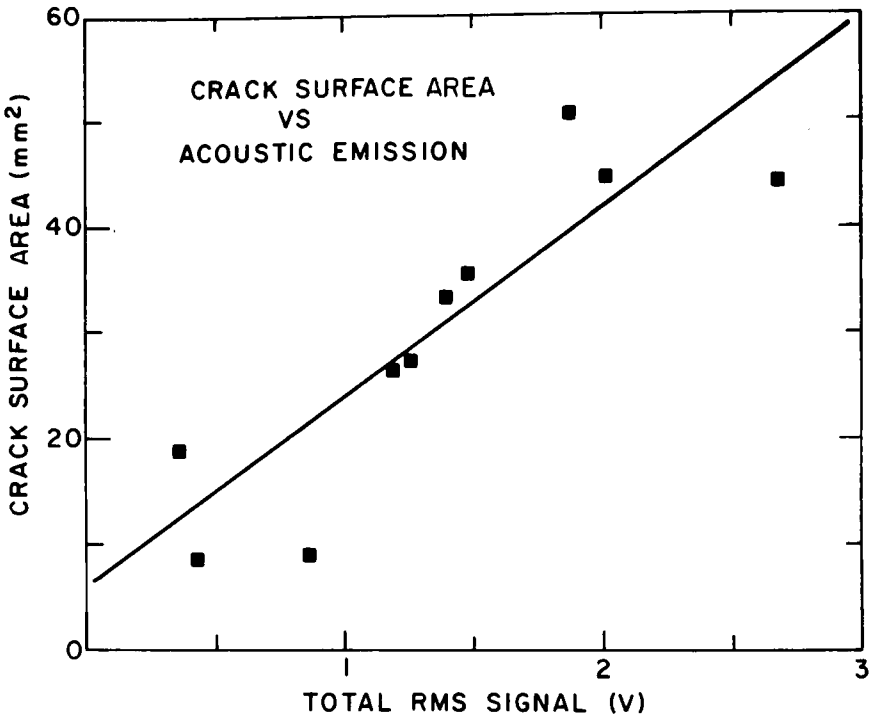

Fig. 16. Crack Surface Area vs Total Rms Signal from Acoustic-emission Monitor. Single pellets were thermally cycled in the DEH apparatus to generate the cracks. Neg. No. MSD-62576.

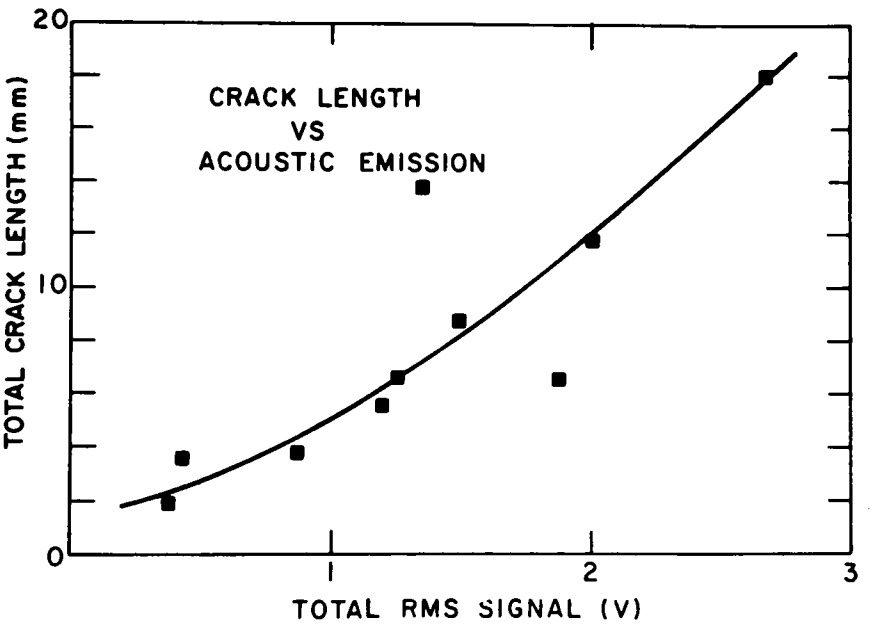

Fig. 17. Total Crack Length vs Total Rms Signal from Acoustic-emission Monitor. Single pellets were thermally cycled in the DEH apparatus to generate cracks. Crack lengths were determined by measurements at the ends of the pellet. Neg. No. MSD-62573.

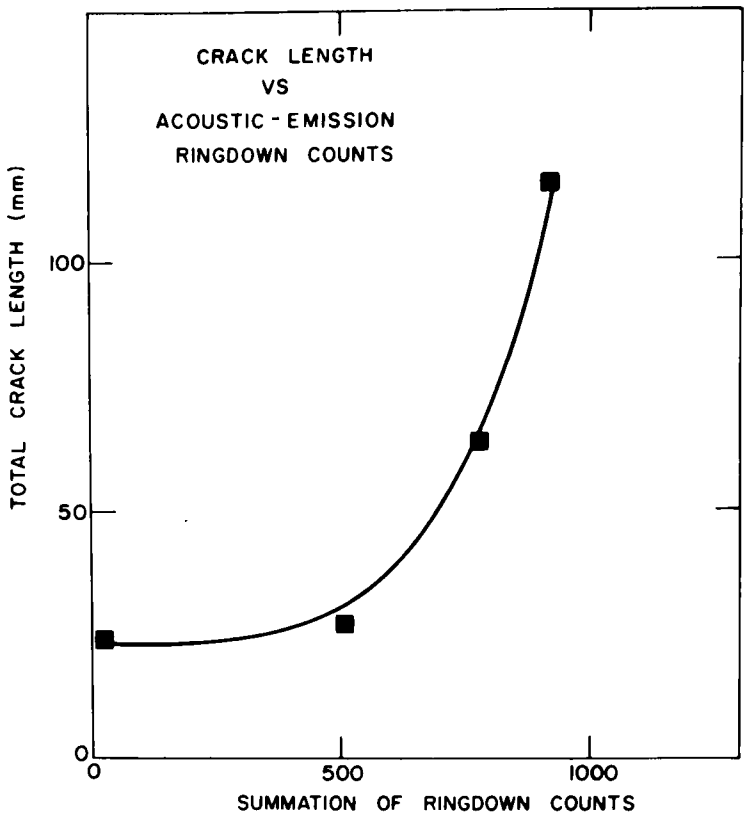

Fig. 18. Total Crack Length vs Summation of Ringdown Counts for Single-pellet Runs. Neg. No. MSD-63473.

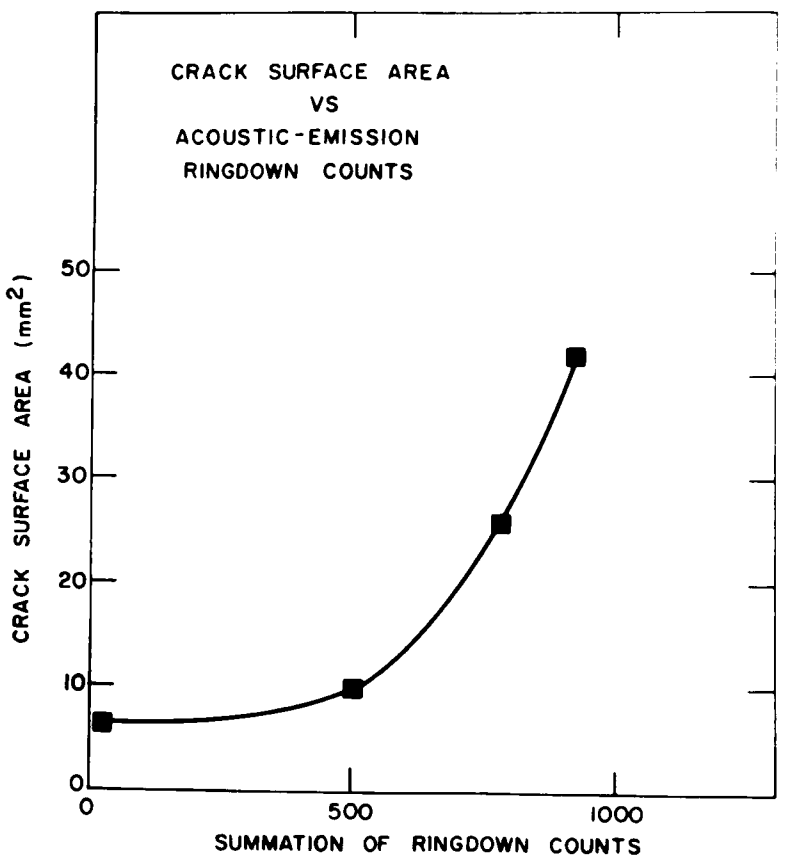

Fig. 19. Total Surface Area vs Summation of Ringdown Counts for Single-pellet Runs. Neg. No. MSD-63474.

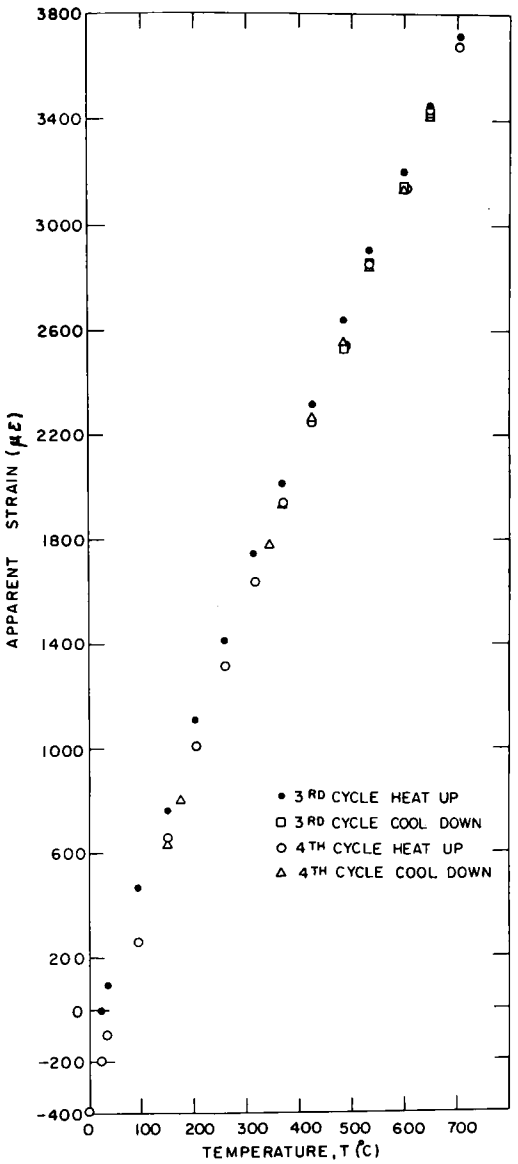

Fig. 20. Apparent Strain as a Function of Temperature. Neg. No. MSD-63047.

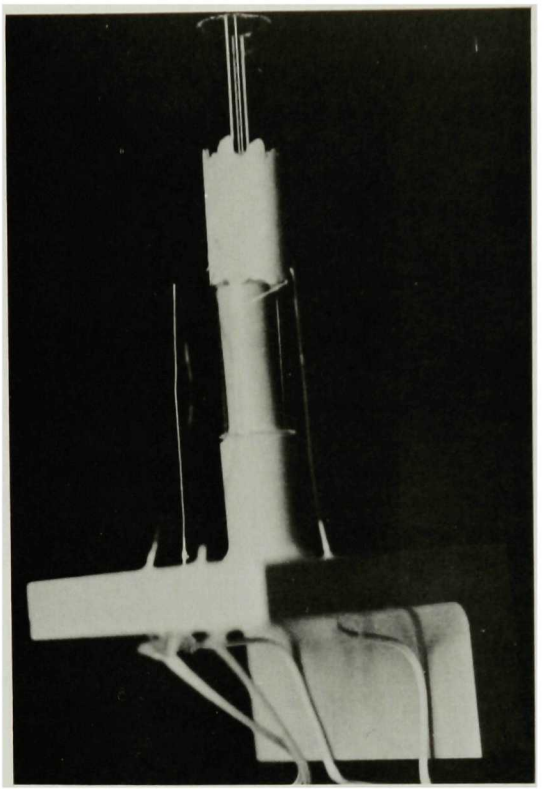

Fig. 21. Fused Silica Cylinder with High-temperature Strain Gauge and Thermocouple Attached Prior to Inserting in Furnace for Apparent Strain Measurements. Neg. No. MSD-63046.

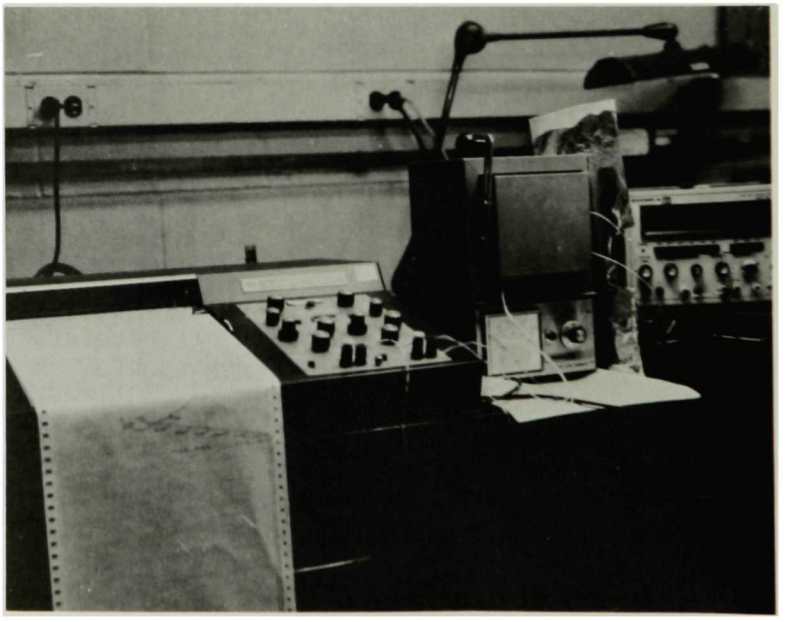

Fig. 22. Test Apparatus for Apparent Strain Measurements. Neg. No. MSD-63045.

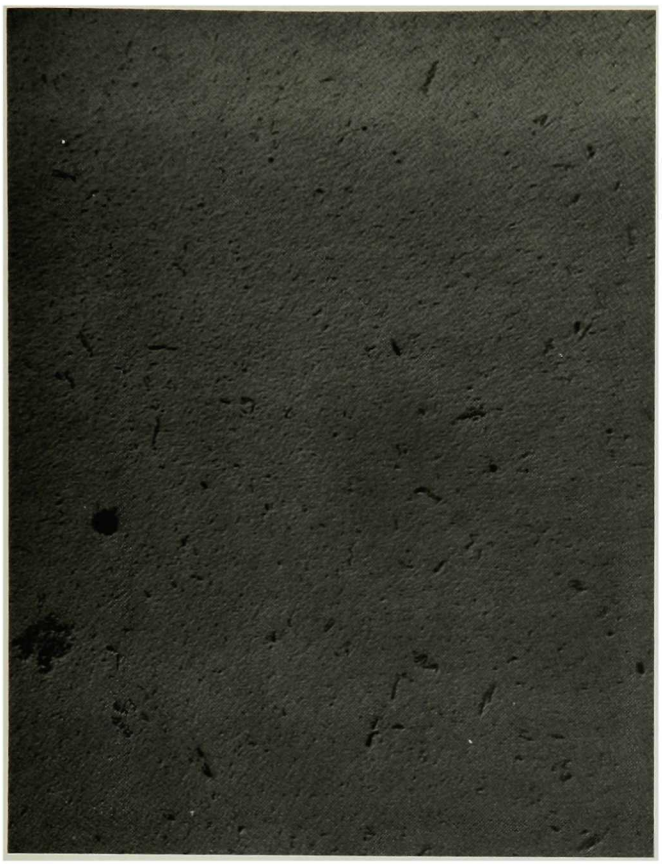

Fig. 23. Micrograph of a Polished Sintered Pellet Showing Pore Size and Shape. Picture width is 2.71 mm (0.11 in.). ANL Neg. No. 306-76-286.

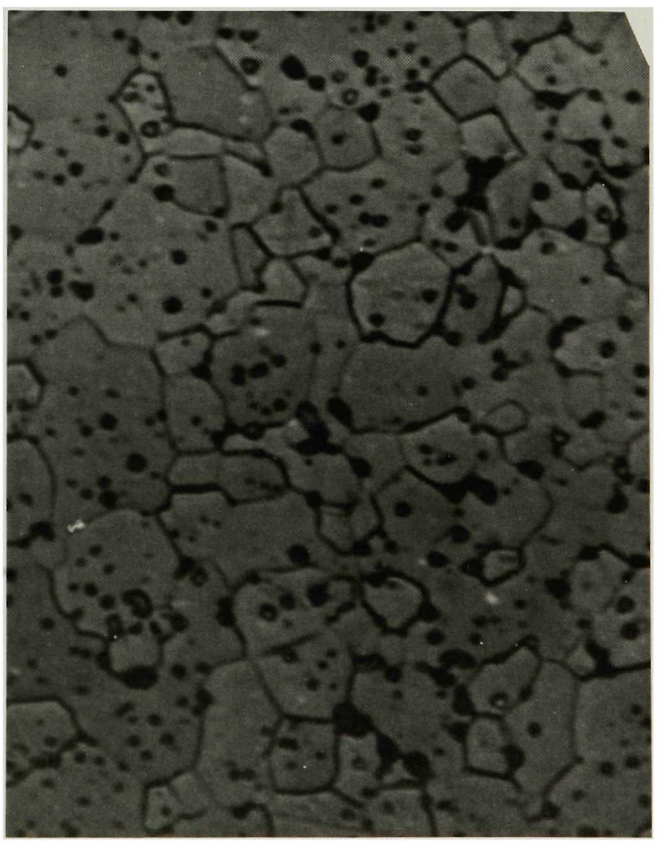

Fig. 24. Micrograph of a Polished and Etched Sintered Pellet Showing Grain Size. Picture width is 44.9 μm (1.77×10^{-6} in.). ANL Neg. No. 306-76-287.

Fig. 25. Micrograph of a Polished and Etched Sintered Plate Showing Grain Size. Picture width is 44.9 μm (1.77×10^{-6} in.). ANL Neg. No. 306-76-288.

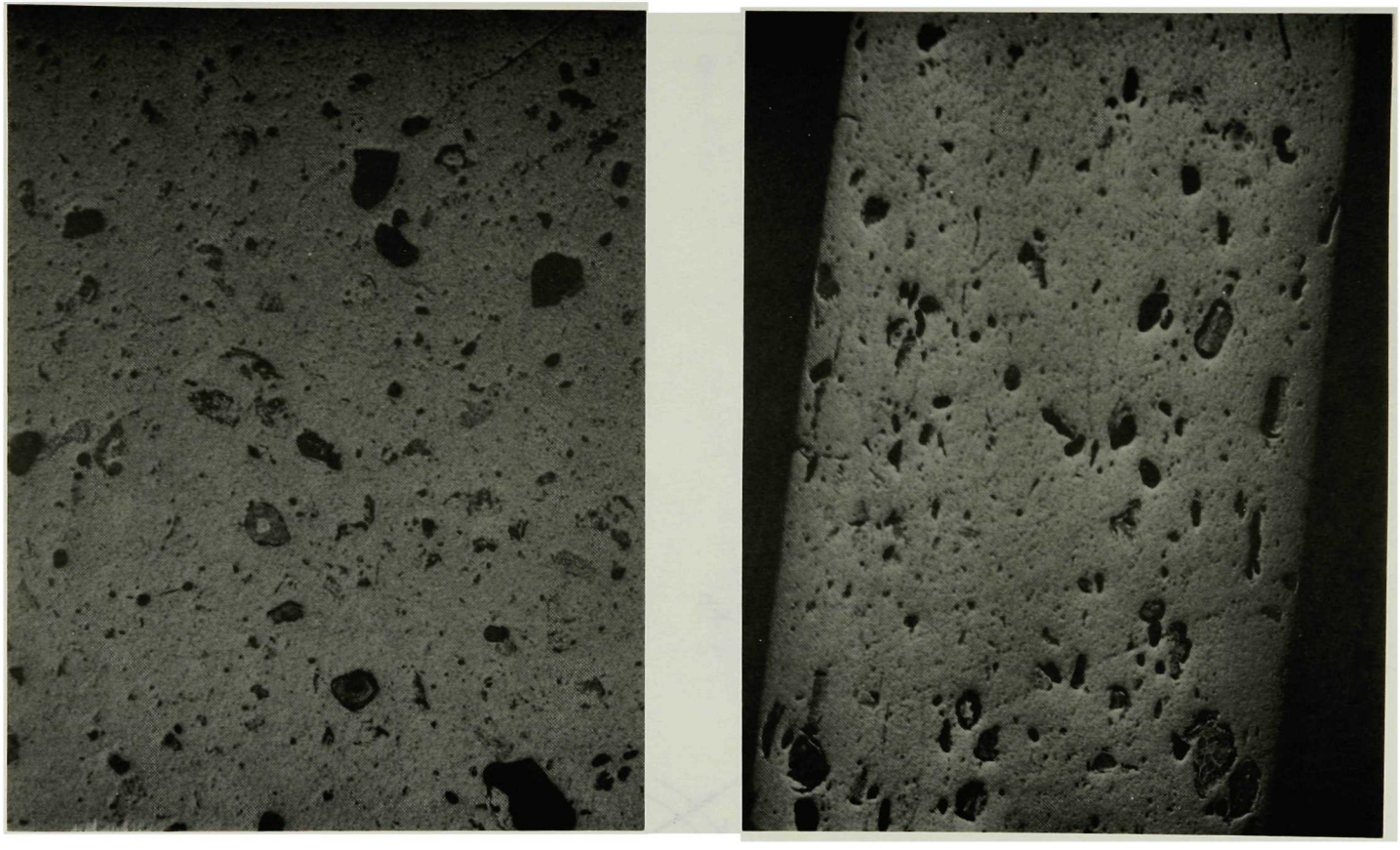

(a) (b)

Fig. 26. Micrographs of Polished Sintered Plates Showing Pore Sizes and Shapes. (a) Perpendicular and (b) parallel to the pressing direction. Picture width is 2.71 mm (0.11 in.). ANL Neg. No. 306-76-289.

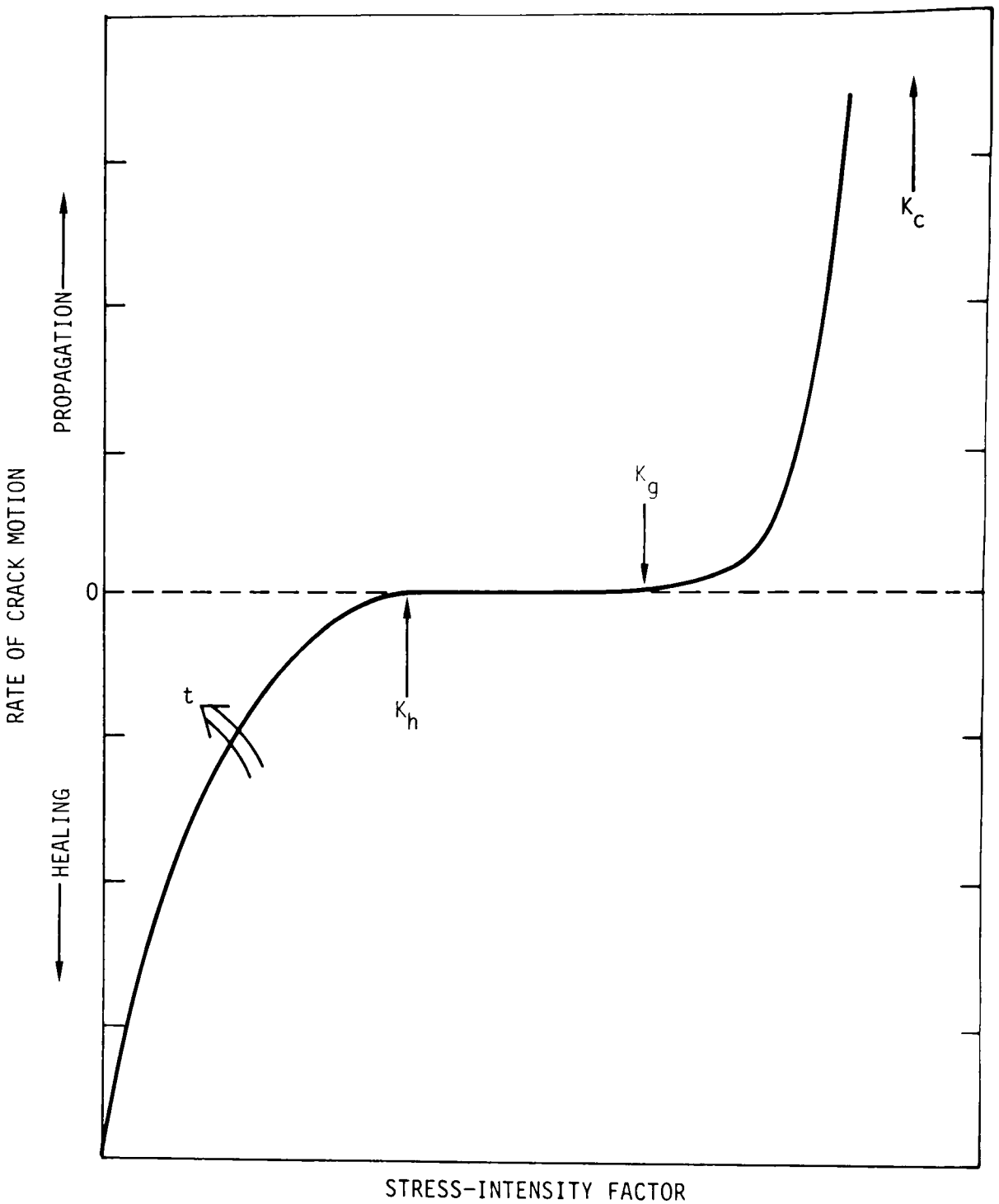

Fig. 27. Schematic of the Dependence of Crack-propagation and Crack-healing Rates on Stress-intensity Factor and Time t.

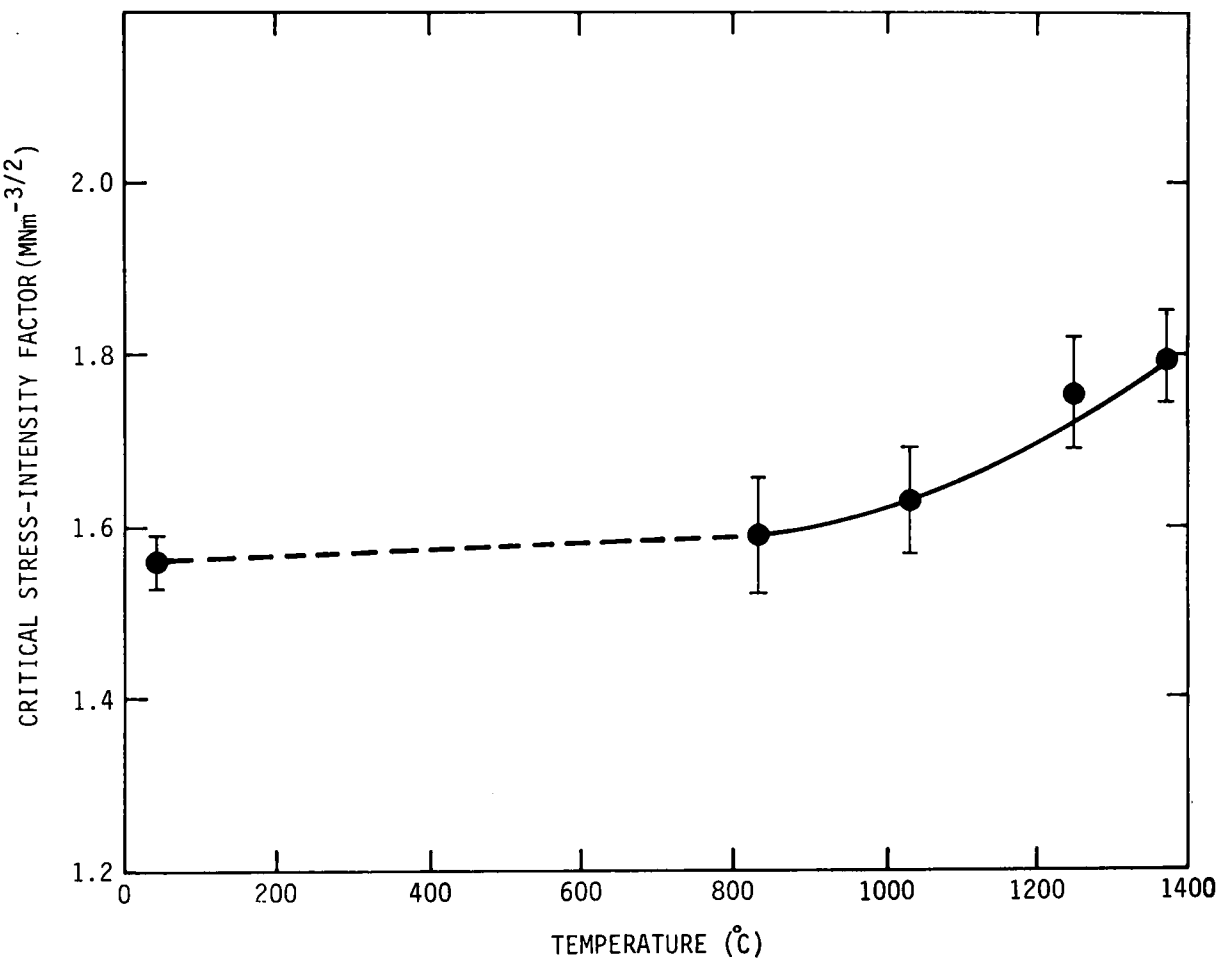

Fig. 28. Temperature Dependence of the Critical Stress-intensity Factor for Sintered UO_2.

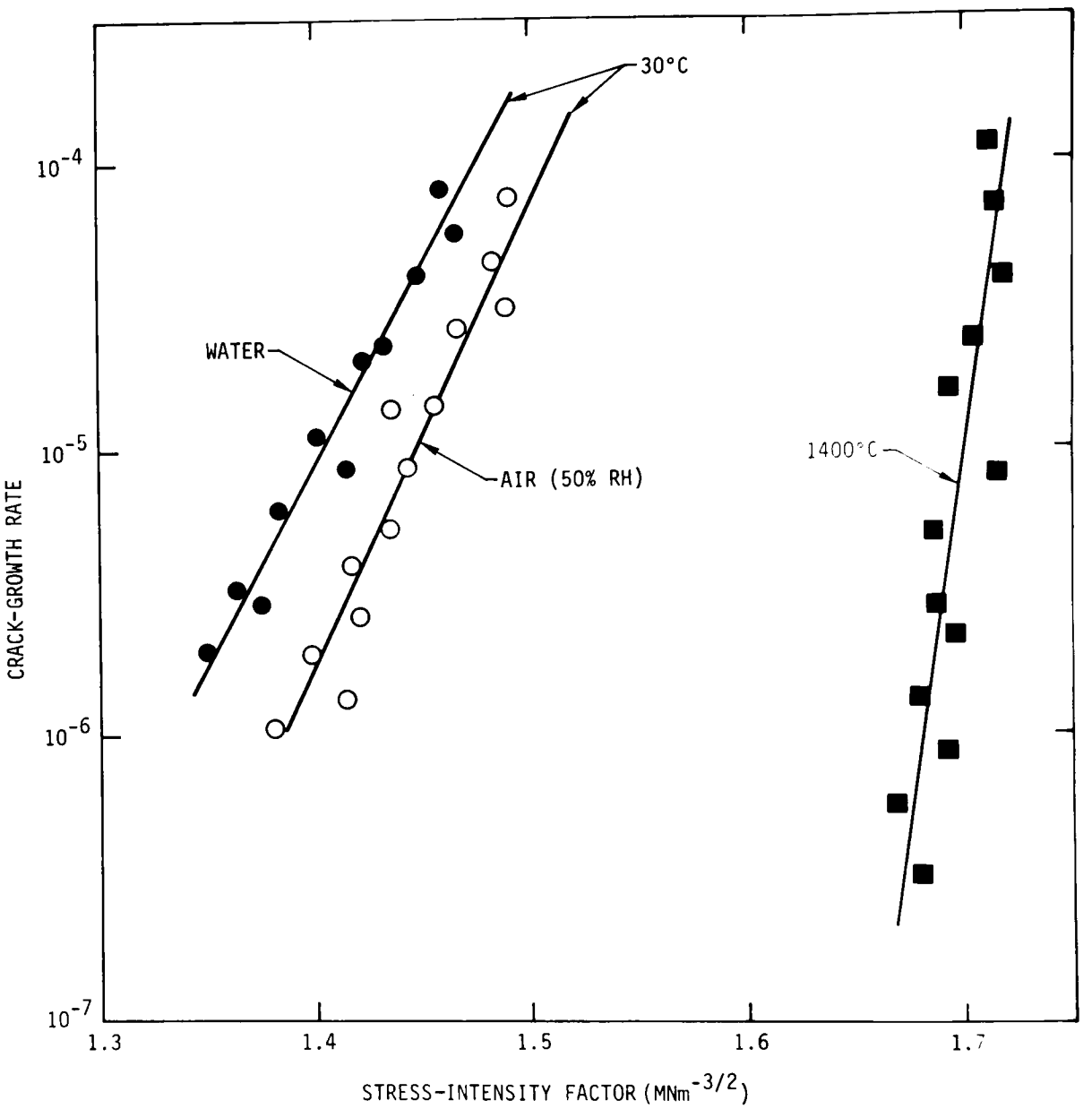

Fig. 29. Slow Crack-propagation Data for UO_2. RH is relative humidity.

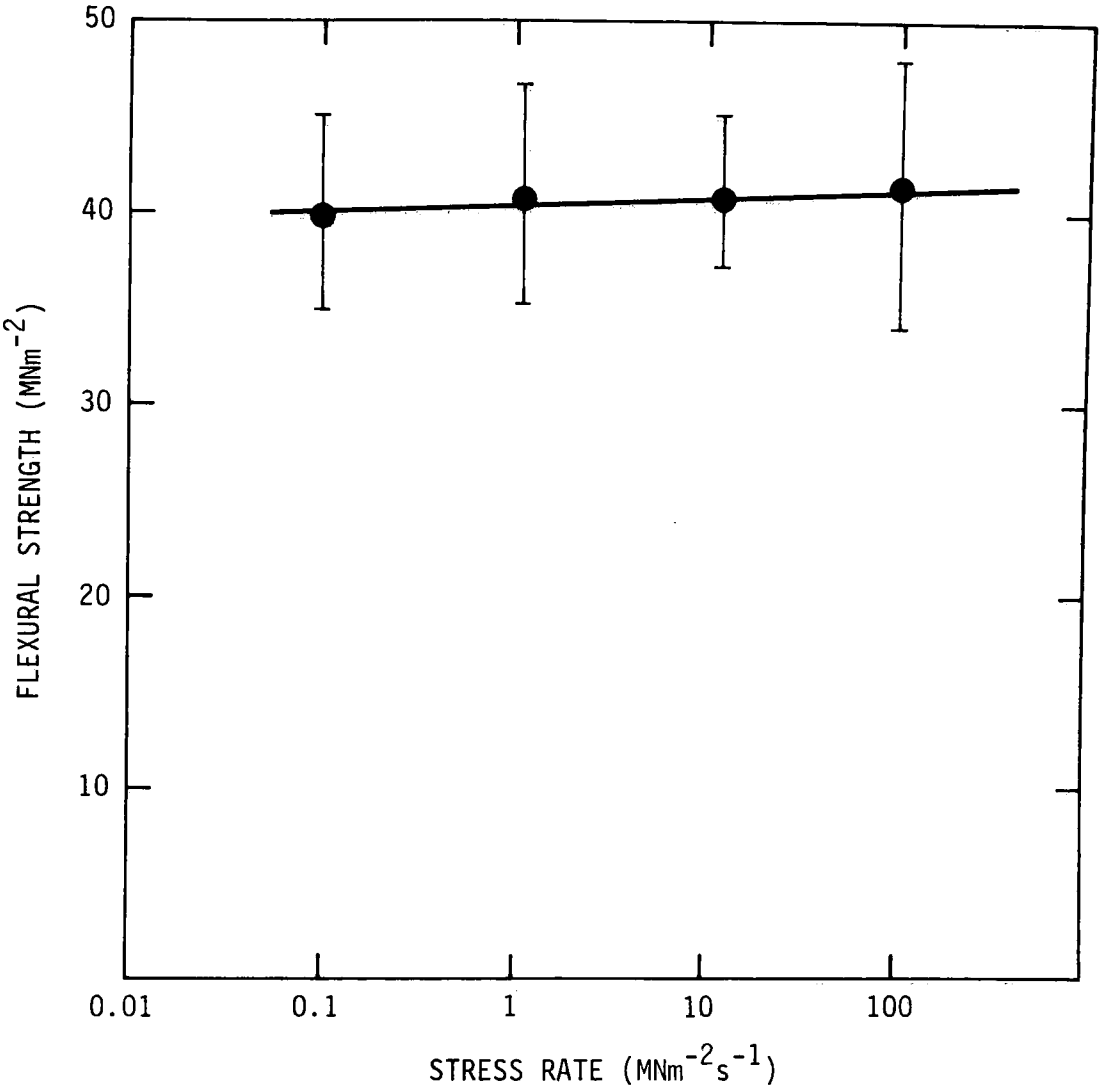

Fig. 30. Stress-rate Dependence of the Strength of Notched Flexure Bars at 1400°C.

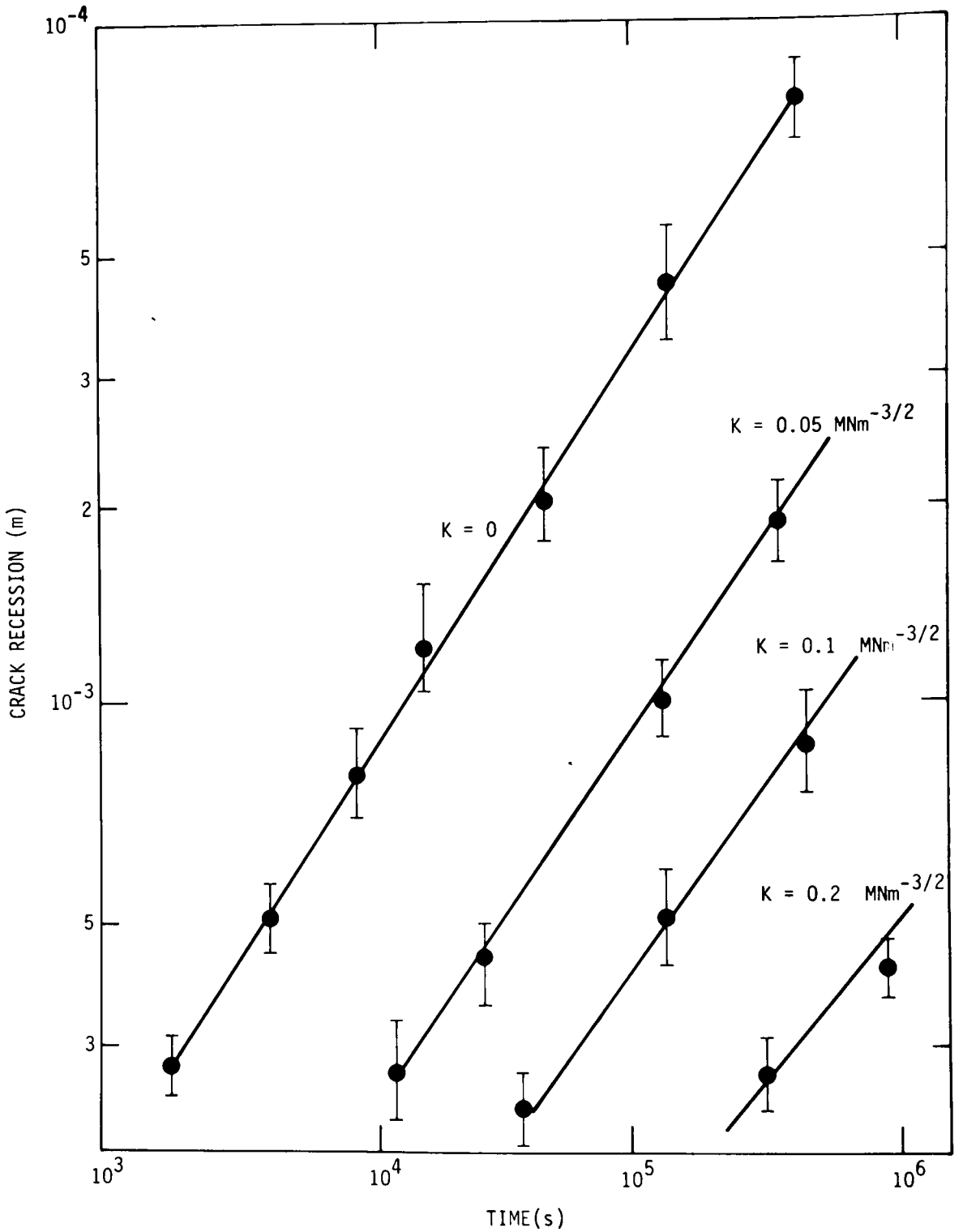

Fig. 31. Time and Stress-intensity Factor Dependence of the Surface Crack Recession at 1400°C.

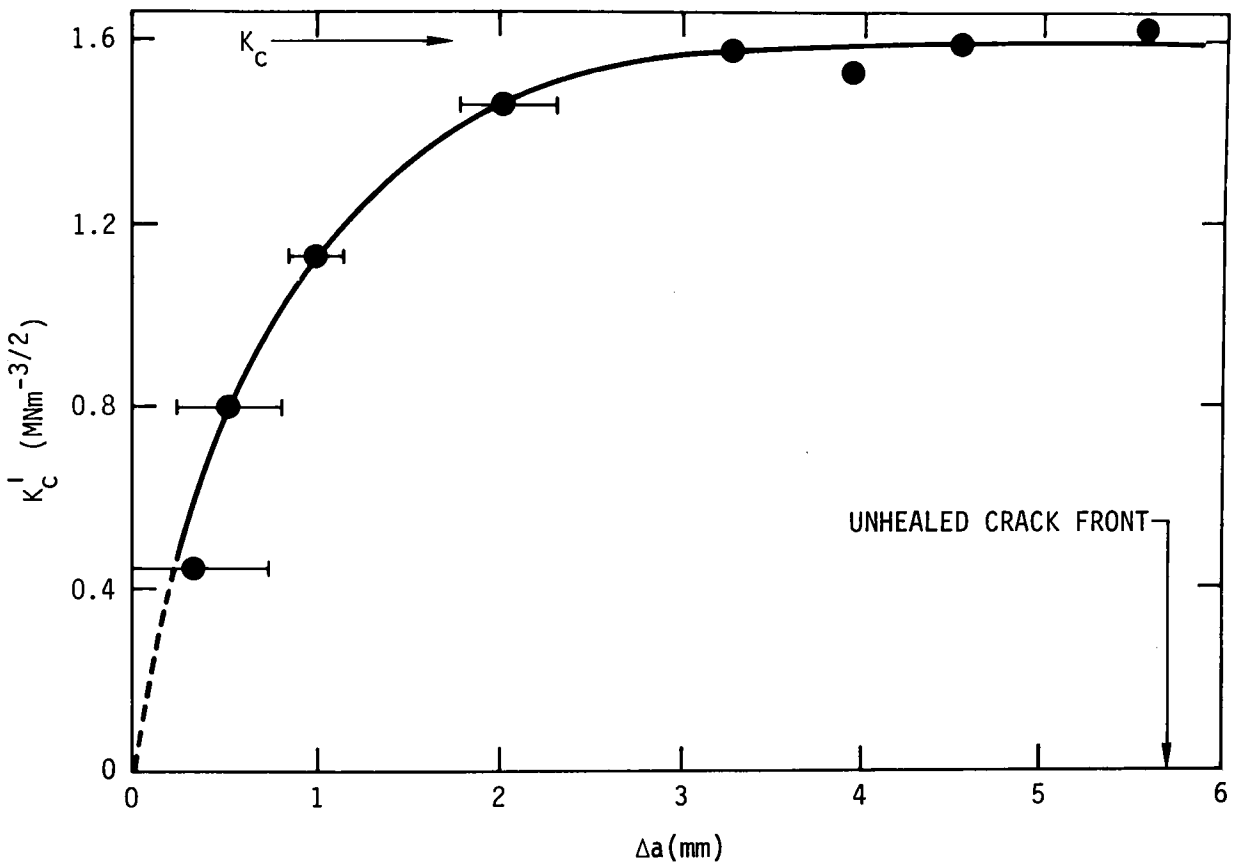

Fig. 32. Change in Critical Stress-intensity Factor with Crack-length Increment, Δa, in Partially Healed Sample Tested at Room Temperature.

Distribution of ANL-76-110

Internal:

M. V. Nevitt
A. Amorosi
R. Avery
L. Burris
A. V. Campise
S. A. Davis
D. C. Rardin
R. G. Staker
R. J. Teunis
C. E. Till
R. S. Zeno
D. C. Price
C. R. Kennedy
F. L. Yaggee
J. C. Voglewede
D. S. Kupperman
B. J. Wrona
W. A. Ellingson
E. Johanson
A. G. Evans
B. R. T. Frost
R. W. Weeks
N. L. Peterson
F. A. Nichols
L. T. Lloyd
J. F. Schumar
M. F. Adams (7)
M. C. Billone
T. H. Blewitt
M. B. Brodsky
D. R. Diercks
F. Y. Fradin
A. G. Hins
T. F. Kassner
U. F. Kocks
K. L. Merkle
M. H. Mueller
L. A. Neimark
R. B. Poeppel
R. W. Siegel
D. Stahl
H. R. Thresh
H. Wiedersich
L. R. Kelman
S. W. Kreis
W. D. Tuohig
A. B. Krisciunas
ANL Contract File
ANL Libraries (5)
TIS Files 6)

External:

ERDA-TIC, for distribution per UC-25, -78, and -80, less duplications (288)
Manager, Chicago Operations Office
Chief, Chicago Patent Group
President, Argonne Universities Association
Materials Science Division Review Committee:
  R. W. Balluffi, Cornell U.
  Sebastian Doniach, Stanford U.
  H. L. Falkenberry, Tennessee Valley Authority
  Campbell Laird, U. of Pennsylvania
  David Lazarus, U. of Illinois
  M. T. Simnad, General Atomic
  A. R. C. Westwood, Martin Marietta Labs.
  V. F. Zackay, U. of California, Berkeley
S. Oldberg, Electric Power Research Institute (50)
J. T. A. Roberts, Electric Power Research Institute
Ronald Christensen, Entropy Ltd., Lincoln, MA
Ekki Kreidl, Entropy Ltd., Lincoln, MA